M. Glasgow[1*], B. Schmandt[1], R. Wang[1], Miao Zhang[2], S. L. Bilek[3] and E. Kiser[4]

[1]Department of Earth and Planetary Sciences, University of New Mexico, Albuquerque, NM, USA

[2]Department of Earth and Environmental Sciences, Dalhousie University, Halifax, Nova Scotia, Canada

[3]Department of Earth and Environmental Science, New Mexico Institute of Mining and Technology, Socorro, NM, USA

[4]Department of Geosciences, University of Arizona, Tucson, AZ, USA

*Corresponding author: Margaret Glasgow (mglasgow@unm.edu)

Key Points:

- Seismicity is hosted by short, <3 km, reactivated basement faults with variable strikes and faulting styles
- The fault zone that hosted a M_w 5.3 event in 2011 exhibits low seismicity following shut-in of nearby injection wells in 2015
- Similarity of spatiotemporal-magnitude basin statistics to tectonic sequences suggests earthquakes mainly release stored tectonic stress

Abstract

The Raton Basin is known as an area of injection induced seismicity for the past two decades, but the reactivated fault zone structures and spatiotemporal response of seismicity to evolving injection have been poorly constrained in the past due to scarce public monitoring. Application of a machine-learning phase picker to four years of continuous data from a local array enables the detection and location of ~38,000 earthquakes. The events between 2016-2020 are ~2.5-6 km below sea level and range from M_L<-1 to 4.2. Most earthquakes occur within previously identified ~N-S zones of seismicity, however our new catalog illuminates these zones are composed of many short faults with variable orientations. The two most active zones, the Vermejo Park and Tercio, are potentially linked by small intermediate faults. In total, we find ~60 short (<3 km) basement faults with strikes from WNW to slightly east of N. Faulting mechanisms are predominantly normal but some variability, including reverse dip-slip and oblique-slip, is observed. The Trinidad fault zone that hosted the 2011 M_w 5.3 earthquake is quiescent during 2016-2020, likely in response to decreased wastewater injection after 2012 and the shut-in of two nearby wells in 2015. Unlike some induced seismicity regions with higher injection rates, Raton Basin frequency-magnitude and spatiotemporal statistics are not distinguishable from tectonic seismicity. The similarity suggests that induced earthquakes in the Raton Basin are dominantly releasing tectonic stress.

Plain Language Summary

The Raton Basin, located on the Colorado-New Mexico border, has a low level of historical seismicity but experienced a significant increase of earthquakes in the past two decades, coinciding with increased wastewater injection and coal-bed methane production. We use four years of continuous local seismic data to detect ~38,000 earthquakes from 2016 to 2020. We find that previously identified 10-20 km long zones of seismicity are composed of many shorter faults, <3 km, with variable orientations and slip mechanisms. We observed very little seismicity in the zone that previously hosted the largest earthquake (M_w 5.3) in the basin and attribute this finding to the significant decrease in the wastewater injection in this zone beginning in 2012. Overall, the statistical spatiotemporal behavior of Raton Basin seismicity is not distinguishable from tectonic seismicity. Their statistical similarity suggests Raton Basin seismicity dominantly releases tectonic stress accumulated over geologic time.

Introduction

Human-induced earthquakes present societally relevant hazards and opportunities to study earthquake sequences and seismogenic structures in the central United States at accelerated time scales. The abrupt rise of human-induced earthquakes in the central U.S. began in 2009 and peaked in 2015 (Figure 1a; Keranen & Weingarten, 2018; Weingarten et al., 2015; Langenbruch et al., 2018). Since 2015, seismicity decreased on average for the central U.S. and decreased or plateaued for the strongest contributing regions, e.g., central Oklahoma and Arkansas (Langenbruch et al., 2018; Scanlon et al., 2019). However, a few regions have expanded operations in recent years and are experiencing a rise in seismicity, e.g., west Texas and southeastern New Mexico (Skoumal & Trugman, 2021; Skoumal et al., 2020; Frohlich et al., 2020). Studying how seismicity evolves following the peak of wastewater injection may be informative for future settings.

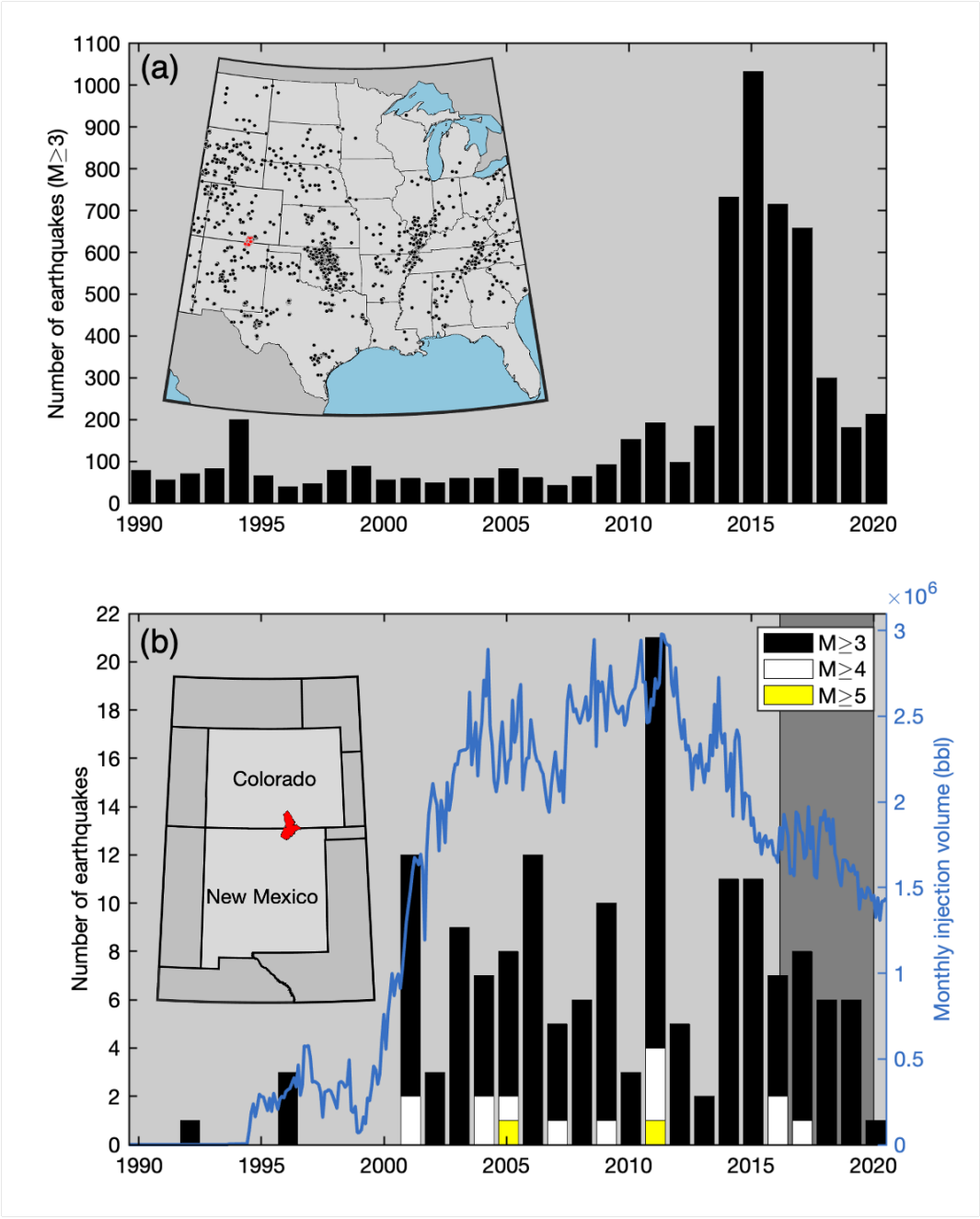

Figure 1. (a) Yearly number of M 3 earthquakes in the central United States (ANSS ComCat, 2021). Inset displays map of the central United States with M 3 earthquakes (circles). Red circles indicate earthquakes in the Raton Basin. (b)

Yearly number of M 3 earthquakes in the Raton Basin. See legend for magnitude. Monthly injection volume (blue line) is on the right y-axis (COGCC, 2021; NMOCD, 2021). Injection is summed across the 24-29 wells typically operating in the basin. Our study period from July 2016 to July 2020 is highlighted in dark gray. Inset displays state borders and the Raton Basin in red.

The Raton Basin located on the Colorado-New Mexico border is one of the central United States regions where seismicity ramped up in concert with wastewater injection (Figure 1b; Rubinstein et al., 2014). Coal-bed methane production and wastewater injection began in 1994 and its increase from ~2000-2002 was accompanied by a rapid increase in seismicity (Figure 1b; Advanced National Seismic System Comprehensive Earthquake Catalog (ANSS ComCat). Thus, the Raton Basin's rise of induced seismicity was ~8 years ahead of the central U.S. average (Figure 1), and it is a valuable example of how induced seismicity persists as injection gradually decreases (e.g., Healy et al., 1968). Historically, seismicity in the basin was rare but not absent. Rubinstein et al. (2014) estimated 3.8 as the Raton Basin's magnitude of completeness from 1970 to 2011. One M 4 earthquake occurred from 1970 to 2000 and 15 M 4 earthquakes occurred from 2001-2020 (Rubinstein et al., 2014; ANSS ComCat, 2021). The rate of M 3 earthquakes in the basin began increasing in 2001 and peaked in 2011. The largest earthquake of the region was the 2011 M_w 5.3 event (Barnhart et al., 2014; Rubinstein et al., 2014). Seismicity decreased over the past several years but remains much higher than prior to 2001 (Figure 1).

The disposal of fluids, generally byproducts of oil and gas production, by injection is a driver of increased seismicity in the central United States (Ellsworth 2013; Keranen et al., 2014; Weingarten et al., 2015). Fluid injection can increase pore pressure and reduce the effective normal stress on faults thereby promoting fault slip (Raleigh et al., 1976). Pore fluid pressure changes of <0.1 MPa are sufficient to induce seismicity (Keranen et al., 2014; Nakai et al., 2017b; Verdecchia et al., 2021). In Oklahoma, southern Kansas, and the Raton Basin, the majority of induced earthquakes occur in the basement beneath the injection reservoir (Walsh & Zoback, 2015; Schoenball et al., 2017b; Nakai et al., 2017b), indicating the presence of permeable pathways between the injection units and basement faults. In Oklahoma and Kansas, Precambrian basement faults extend upward into the primary wastewater disposal unit providing likely pore-fluid pressure pathways (Schwab et al., 2017). In the Raton Basin, it is less certain how pore pressure is transmitted to the basement, but permeable faults have been hypothesized (Rubinstein et al., 2014; Nakai et al., 2017b).

Injection rate and cumulative injected volume are proposed as key parameters that influence induced seismicity (Weingarten et al., 2015; Scanlon et al., 2019; McGarr, 2014). High-rate injection wells (300,000 bbl/month) are associated with earthquakes twice as often as low-rate injection wells (<100,000 bbl/month) (Weingarten et al., 2015). Scanlon et al. (2019) found the association of earthquakes to cumulative wastewater injection volume remained random below 1 million bbl/well and increased from 60% at 1 million bbl/well to ~90-100%

at 30 million bbl/well. The average monthly injection in the Raton Basin is ~80,000-90,000 bbl/well since 2001 and the average cumulative wastewater injection volume is ~22 million bbl/well since 1994 (Figure 1).

Publicly accessible seismic instrumentation near the Raton Basin has been sparse, with the exception of temporary aftershock deployments in 2001 and 2011 (Meremonte et al. 2002; Rubinstein et al. 2014) and the EarthScope Transportable Array (TA) during which two stations bounded the basin from 2008-2010 (Nakai et al., 2017a; 2017b). Previous seismic studies identified three prominent zones of seismicity (Figure 2), referred to as the Trinidad (Rubinstein et al., 2014; Barnhart et al., 2014), Vermejo Park, and Tercio zones (Nakai et al., 2017b). The Trinidad zone strikes NE-SW, extends ~15 km, and hosted a M_w 5.3 earthquake in 2011, the largest recorded within the basin (Rubinstein et al., 2014). The Vermejo Park and Tercio zones strike N-S and extend ~20 and ~10 km, respectively (Nakai et al., 2017b). It is unclear if these zones are spanned by continuous faults. Recent research with a dense one-month array in a subset of the Raton Basin suggests that more complex fault networks exist within the previously identified zones of seismicity (Wang et al., 2020).

Deployment and continuous operation of a local broadband array since 2016 (Figure 2) allows this study to advance knowledge of the structural setting and the spatiotemporal characteristics of Raton Basin seismicity in the context of post-peak wastewater injection. A new high-resolution earthquake catalog was built by taking advantage of a machine-learning phase picker (Zhu & Beroza, 2019) and waveform correlation based hypocenter estimation method (Trugman & Shearer, 2017) to investigate four years of continuous seismic data. The new catalog of ~38,000 events is quantitatively analyzed to constrain the geometry of reactivated faults, whose diverse orientations are supported by complementary focal mechanism analysis. Spatiotemporal-magnitude statistics are calculated for multiple sections of the basin and compared to results from tectonic and other induced settings to evaluate potential drivers of Raton Basin seismicity.

Geologic background

The Raton Basin is asymmetric with the syncilinial axis west of center (Johnson & Finn, 2001). The western margin dips steeply east toward the Sangre de Cristo Mountains, whereas the eastern margin tilts gently west (Woodward, 1996; Johnson & Finn, 2001; Flores & Bader, 1999; Baltz, 1965). Devonian through Plio-Pleistocene basin stratigraphy is underlain by Precambrian basement (Johnson & Finn, 2001). East-west compression during the Laramide orogeny (late Cretaceous to early Tertiary) resulted in predominantly ~N-S oriented faults and fold axes (Woodward, 1996). Sills and steeply dipping dikes were emplaced during the mid to late Tertiary following the weak zones created during the Laramide orogeny (Johnson, 1969; Johnson & Wood 1956; Woodward, 1996). Evidence of the widespread intrusive activity includes over 80 mapped dikes and sills (Johnson, 1969; Dane & Bachman, 1965, Woodward,

1996) and the Spanish Peaks (Figure 2) towering with ~1.5 km of structural relief over the basin (Johnson & Finn, 2001). Many intrusive features are perpendicular to the syncline shown in Figure 2 (Papadopulos & Associates, 2008; Woodward, 1996). The exceptions are radial diking in the northwest basin and sills which outcrop as cliffs and follow topographic contours (Figure 2). Dike thicknesses vary from centimeters to >30 m (Flores & Bader, 1999) and likely intruded preexisting fractures formed during hydrocarbon generation (Woodward, 1996).

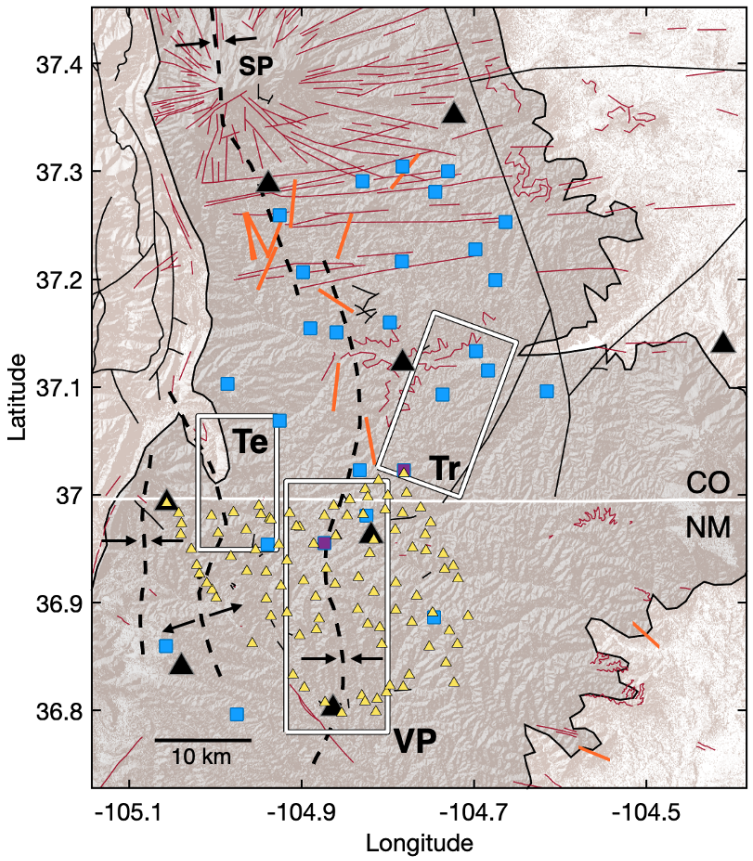

Figure 2. Map of study region. The Raton Basin is outlined in black and shaded gray. The eight broadband seismometers (black triangles), 96 geophone nodes (yellow triangles), and 29 wastewater injection wells (blue squares) used in this study. Purple squares indicate collocated wastewater injection wells. The three white boxes approximate previously identified zones of seismicity from Rubinstein et al., (2014) and Nakai et al., (2017). They are abbreviated Te

– Tercio, Tr – Trinidad, and VP – Vermejo Park. Geologic features include mapped surface faults (black lines), mapped dikes and sills (red lines), and anticlines and synclines (dashed black lines). The Spanish Peaks are labeled SP. Orange lines are maximum horizontal stress orientations from Lund Snee and Zoback, (2020).

The N-S normal faulting extensional stress field of the Rio Grande Rift converges with the E-W strike-slip compressive stress field of the broader central United States at the Raton Basin (Lund Snee & Zoback, 2020) producing a range of stress orientations, NE-SW to NW-SE maximum horizontal stress, in and along the margins of the basin (Figure 2). Earthquake focal mechanisms support predominantly normal dip-slip and occasional strike-slip motion near the central basin (Barnhart et al., 2014; Wang et al., 2020; USGS National Earthquake Information Center; St. Louis University, http://www.eas.slu.edu/eqc/). Similar to the neighboring Rio Grande Rift and southern Rocky Mountains, the Raton Basin has high heat flow, ~90 mW/m^2 (Blackwell et al., 2011).

Data

Data from two seismic arrays (Figure 2) are used to investigate Raton Basin seismicity from July 2016–July 2020 (Table S1). The first is an eight-station broadband with ~30 km inter-station spacing and continuous 100 Hz sampling. Seven of the stations were deployed in 2016 (Table S1, UNM1-7). The eighth station, T25A, is a legacy Transportable Array station located near the eastern edge of the basin. The second array is composed of 96 Fairfield-Magseis 3-C nodes deployed in the southern portion of the basin from May–June 2018 (Figure 2, Table S1). The nodes contain 5-Hz geophones. They were spaced ~2-5 km apart and recorded continuously with a sample rate of 250 Hz.

Publicly available wastewater injection volume data are used to investigate spatial and temporal changes in injection volume for the Raton Basin. Public injection records are accessible through online databases by state, the Colorado Oil and Gas Conservation Commission (COGCC, 2021) and New Mexico Oil Conservation Division (NMOCD, 2021). The monthly injection volume is reported for each well in Colorado (CO) since 1998 (COGCC, 2021) and in NM since 2006 (NMOCD, 2021). We refer to Rubinstein et al. (2014) for the yearly cumulative wastewater injection volume in New Mexico (NM) prior to June 2006. The number of active wells in the basin varies from 24-29 (Figure 2). The current metadata indicates that one well (VPR 007) in NM is located ~30 km west of the basin (NMOCD, 2021) but previous publications (e.g., Nakai et al., 2017b; Rubinstein et al., 2014) indicate VPR 007 as collocated with VPR 042. Based on prior publications and Google Earth satellite imagery, we consider well VPR 007 to be within 100 m of VPR 042, located in the northwestern part of the Vermejo Park zone (Figure 2, purple square). Two other collocated wells are reported in the southernmost Trinidad zone (Figure 2). When considering injection volume, wells within 100 m are summed.

Methods

4.1 Event detection and location

1. **Detection and event association**

A deep neural network package called PhaseNet was used to estimate the probabilities of earthquake P and S arrivals within continuous unfiltered seismic data (Zhu & Beroza, 2019). PhaseNet was trained on >600,000 recordings from the Northern California Earthquake Data Center Catalog and has been successfully applied in many regions (e.g., Liu et al., 2019; Park et al., 2020) including the southern portion of the Raton Basin (Wang et al., 2020). All resulting phase detections with a probability 0.3 for the broadband array (Figure 3, e-f) and 0.5 for the 1-month node array were passed to the event association step, which was performed using the Rapid Earthquake Association and Location algorithm (REAL, Zhang et al., 2019) with the 1-D velocity model from Wang et al. (2020). A minimum of five total phases were required for event association, including at least three P and two S arrivals. Higher thresholds were required during the month of the 96-node array, with 50 phases including at least 25 P and 10 S arrivals. We set a higher requirement on the number of phase picks because the primary goal of including the node data is to better constrain hypocenters for clusters active during that month rather than to increase the number of earthquake detections. For a focused study on detecting earthquakes during the month of the node array see Wang et al., (2020).

More manual phase picking was also conducted using short-term average to long-term average detections (Allen, 1978; Earle and Shearer, 1994) followed by analyst adjustment of P and S picks. There are ~5,500 earthquakes in the manually refined earthquake catalog from July 2016–May 2019 and ~25,000 earthquakes in the automated catalog for the same time period. Comparing >50,000 picks between the automated and manually refined results reveals that 98% of P and 94% of S phase picks are within one tenth of a second. Automated picks are slightly (0.018 s on average) earlier than manual picks (Figure 3a & d). The automated approach results in an ~4.5-fold increase in the number of events detected.

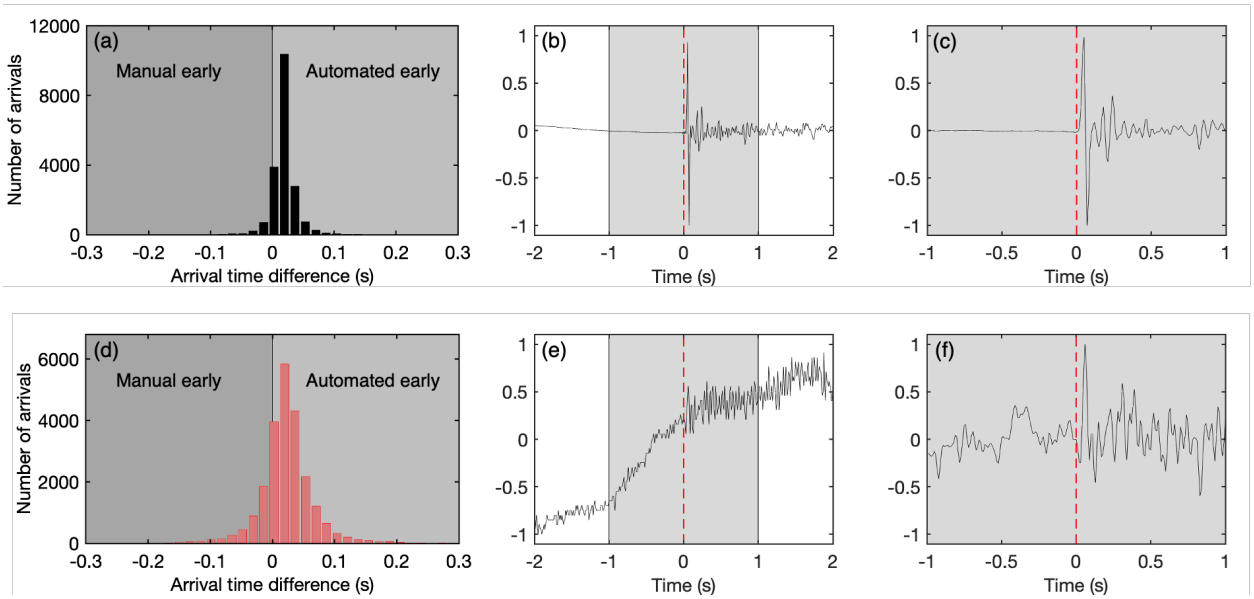

Figure 3. PhaseNet earthquake arrival time results and examples. (a) P and (d) S phase distributions of arrival time differences between manual and automated approaches. (b-c, e-f) Normalized waveforms for events with different probability P arrival (red dashed line) from PhaseNet (Zhu & Berosa, 2019). (b, e) show unfiltered waveforms. (c, f) show zoomed and corresponding waveforms filtered between 1-20 Hz. b-c) high (0.99) and (e-f) low (0.3) probability.

4.1.2 Hypocenter estimation

Initial locations from REAL were refined using VELEST, a least-squares absolute hypocenter estimation method (Kissling et al., 1994). The 1-D velocity model from Wang et al. (2020) was used to estimate hypocenters. The earthquake catalog with absolute locations from VELEST includes 37,866 earthquakes from July 2016–July 2020 (Figure 4).

The catalog was relocated using GrowClust (Trugman & Shearer, 2017), which relies on waveform similarity to cluster earthquakes and estimate relative locations with correlation based differential times. The 1-D velocity from Wang et al. (2020) was used with GrowClust. Prior to cross-correlation, bandpass filtered (1-20 Hz) waveforms were cut from -1 to 1.5 s for P arrivals and -1 to 2.5 s for S arrivals similar to Trugman and Shearer (2017). The East or North horizontal channel with the higher correlation was used for S. Each earthquake was correlated with its 300 nearest neighbors. A range of cluster connectivity and correlation threshold parameters was tested (Figure S1) because they affect the spatial compactness and splitting of hypocenter clusters. The orientation of earthquake clusters remained fairly consistent between parameter tests (Figure S1). Only event pairs with cross correlation coefficients 0.5 are considered. For final results, the connectivity ratio was set to 0.01 and a minimum of 5 phases

with cross-correlation coefficients 0.6 were required (Figure 4, b & e). Sixty percent (22,684 of 37,866) of the earthquakes were relocated (Figure 4b), including 91 clusters with >50 earthquakes and 46 clusters with >100 earthquakes. Growclust's nonparametric error estimate was used to estimate the horizontal and vertical location error. The median horizontal and vertical earthquake location errors are 180 m and 240 m, respectively, following 100 bootstrap resamples.

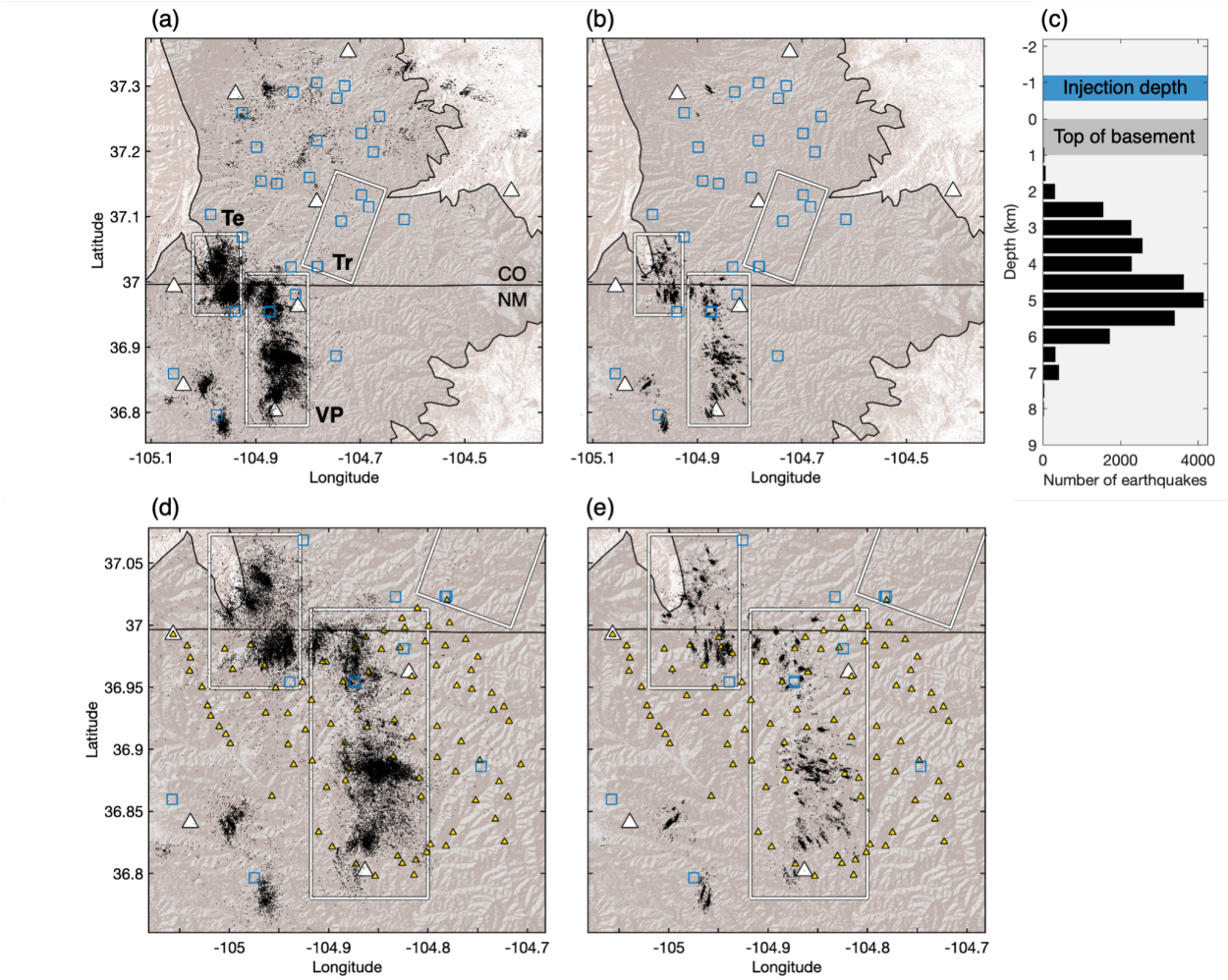

Figure 4. Earthquake locations. The basin is outlined in black. The state border is a black line. The white boxes outline regions of seismicity identified by past studies (Nakai et al., 2017; Rubinstein et al., 2014). They are abbreviated Te – Tercio, Tr – Trinidad, and VP – Vermejo Park in (a). (a) Absolute location of earthquakes (black dots) and (b) relative relocation of earthquakes (black dots). (c) The depth distribution of relative relocation earthquakes from (b). (d) and (e) zoom in on the most seismically active regions from (a) and (b)

respectively. White triangles are broadband seismometers. Blue squares are wastewater injection wells. Yellow triangles are geophone nodes.

4.2 Local magnitude calculation

Three-component waveforms were filtered from 0.01 – 40 Hz, corrected for instrument response, and converted to Wood-Anderson displacement. Waveforms were cut 0.5 s prior to the P arrival to 3 s after the S arrival for local magnitude (M_L) calculations (Gutenberg & Richter, 1956). To maintain consistency throughout the four-year catalog, only broadband waveforms were considered for magnitude calculation. The maximum three-component vector amplitude (A) and the distance from each station to the earthquake (D) are used to calculate the local magnitude for each arrival at each station. The magnitude formula (Gutenberg & Richter, 1956). was calibrated with the 10 largest earthquakes from full waveform moment tensor inversions:

$$M_L = \log_{10}(A) \ + 2.56 \log_{10}(D) \ - 4.69$$

The final estimate is the median of all station M_L for the event.

4.3 Fault determination

Two-dimensional principal component analysis (PCA) was used to estimate the strikes of clusters with 40 earthquakes or more. The distance of stations to earthquakes and the small range of earthquake depths (Figure 4c) deter us from using three-dimensional PCA to estimate fault dip. Bootstrap resampling with 100 iterations was used to reduce the effect of potential outliers on PCA results and estimate strike uncertainties. Only mean strikes with one standard deviation $<10°$ are accepted. In addition, we rejected clusters with the first principal component less than two times greater than the second principal component. In total, 57 clusters passed the criteria for strike estimation (Figure 5).

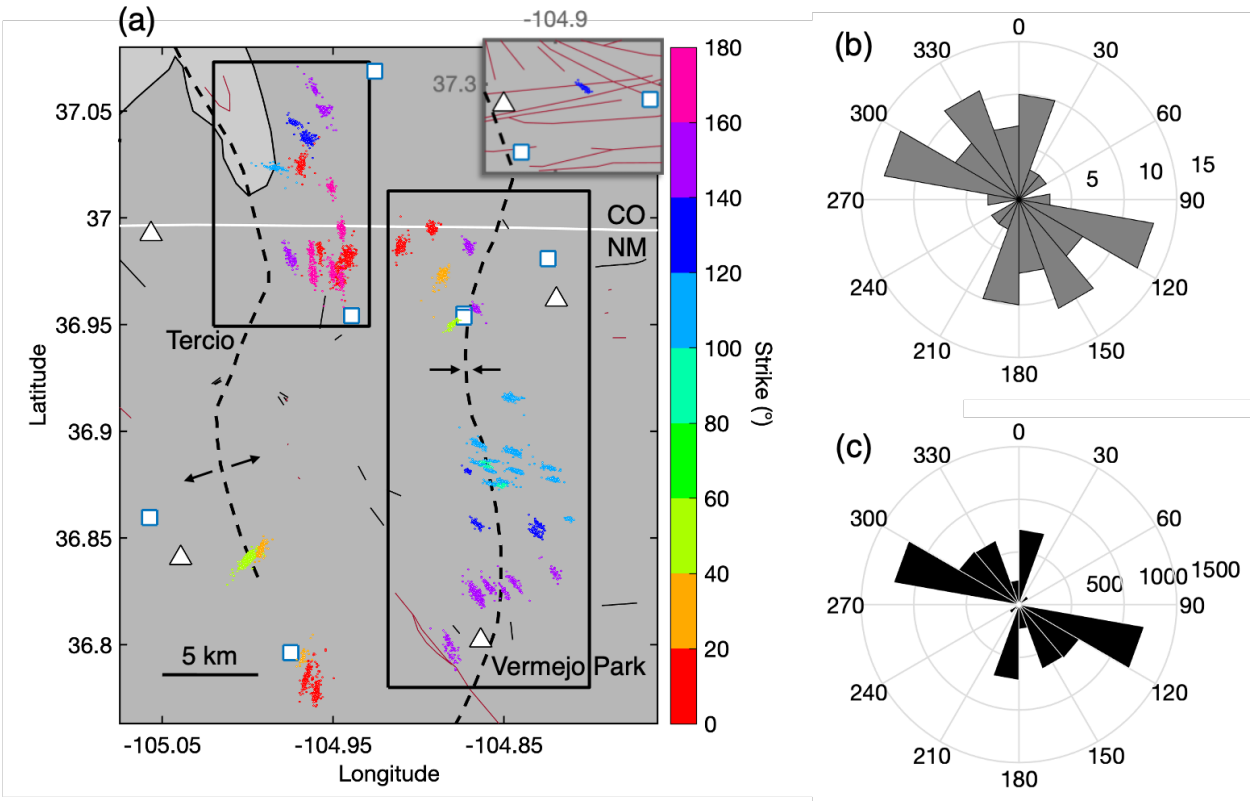

Figure 5. Estimated fault orientations. (a) Dots mark earthquake hypocenters and color corresponds to the estimated strike of the hypocenter cluster based on principal component analysis (PCA). The inset shows the single cluster located outside of the main figure region. Surface geology includes faults (thin black lines), dikes (red lines), synclines and anticlines (black dashed lines). The Tercio and Vermejo Park zones (black boxes) are labeled. Triangles are seismometers and squares are wastewater injection wells active during 2016 to 2020. The basin has a dark gray background and a black outline. (b) A summary of the strike distribution of the estimated faults from PCA in (a). (c) The distribution of M_L>0.5 earthquakes from (a) by fault strike.

4.4 Source mechanism constraints

Deviatoric moment tensors were estimated for 27 M 2.8 earthquakes, which produced low-frequency waveforms suitable for inversion with the Time Domain Seismic Moment Tensor (TDMT) package (Dreger, 2003). The same 1-D velocity model used for hypocenter estimation (Wang et al., 2020) was used to calculate a Green's function library for TDMT inversions. A frequency band of 0.08-0.4 Hz was used and the window length varied between 10 to 15 s, depending on the source-receiver distance. The parameter choices were inherited from

previous studies in a similar setting (e.g., Wang et al., 2016, 2017). Although only 8 stations are available, they are all within ~50 km and approximately evenly distributed so azimuthal gaps are limited for events within the Raton Basin. Even the 2 out of 27 events inverted with 4 stations showed mechanisms comparable to those estimated from larger events nearby. The average variance reduction for TDMT inversion results is 66% and the highest is 90%. Event epicenters were taken from the newly developed catalog and depths were independently optimized based on a grid-search with 1-km increments. The depths estimated with moment tensor inversions are consistent with the catalog, with a mean difference of 0.26 km (±1.58 km).

Some highly active clusters did not host M 2.8 events during the study period therefore they were investigated with focal mechanism estimates using first-motion polarities (i.e., FOCMEC; Snoke, 2003). One of the key targets for first-motion focal mechanism analysis was the concentration of hypocenter clusters with strikes of ~100° located in the center of the previously identified ~N-S Vermejo Park zone (Figure 5). Additionally, two prominent clusters within the Tercio zone (Figure 5) were investigated. As a result, four additional focal mechanisms are included in Figure 6 (purple beach balls). These events with M_L between 1.26-2.33 provided between 70-92 clear first-motion polarity picks (Figure

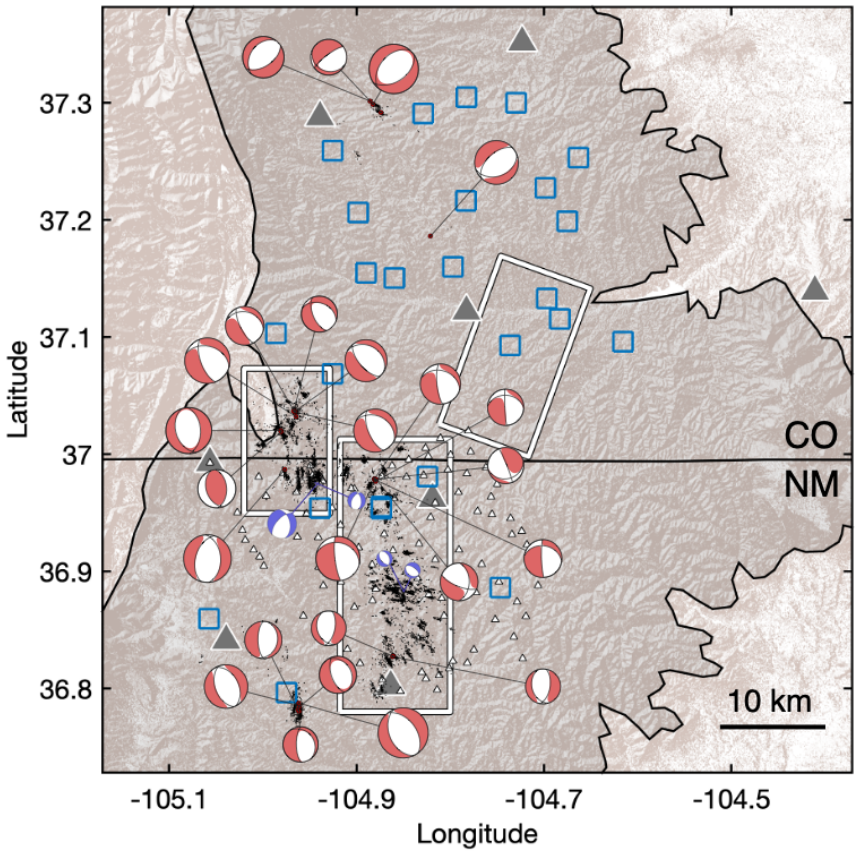

S2).

Figure 6. Source mechanism constraints. Deviatoric moment tensor inversion (red and white) resolved from broadband station (gray triangles) recordings. First-motion polarity based focal mechanism inversion results for four smaller magnitude events (purple and white) resolved using nodal station (small white triangles) recordings. The size of the beachball symbols scales with M_L from 1.26-3.99. From east to west, white boxes mark the Trinidad, Vermejo Park, and Tercio zones. Blue squares are the active wastewater injection wells between 2016-2020. The apparent inconsistency between the moment tensors and hypocenter cluster near 37.3° N is discussed in section 5.2.

4.5 Statistical analysis

Examining the statistical behavior of earthquakes in a region can help discriminate between induced and tectonic sequences (e.g., Zaliapin & Ben Zion, 2016; Schoenball et al., 2015). A variety of statistical analyses are used to investi-

gate how Raton Basin seismicity is distributed in magnitude, time, and space. Each approach was applied to the full basin and three subregions: the northern basin, the Tercio zone, and the Vermejo Park zone (Figure 7). The additional earthquake detections from using the nodal array were not considered to maintain spatiotemporal and magnitude consistency throughout the catalog. The frequency-magnitude distribution is considered first to estimate magnitude of completeness (M_c) and slope of the decay in earthquake frequency with increasing magnitude (b-value). M_c and b-value were estimated using the maximum curvature method (Wiemer and Wyss 2000). A b-value of ~1 is expected given the Gutenberg-Richter law but has been suggested to deviate in non-tectonic regions, including injection-induced (Goebel et al., 2016; Mousavi et al., 2017) and volcanic settings (Roberts et al., 2015; Farrell et al., 2009). Only earthquakes with magnitudes greater than each region's M_c (Figure 8a) are included in the subsequent statistical assessments (e.g., Figure 8c-d).

Spatiotemporal and magnitude clustering of earthquakes were investigated using three approaches: inter-event time distributions, optimized Epidemic Type Aftershock-Sequences models (ETAS; Ogata, 1988), and nearest neighbor space-time distributions (Zaliapin & Ben-Zion, 2016). First, inter-event times indicate the temporal clustering of earthquakes and are quantified by the average coefficient of interevent time variation (C_V). C_V is ~1 for Poisonnian processes (e.g., independent background events), and C_V>4 is expected for highly clustered earthquakes (e.g., aftershocks) (Schoenball & Ellsworth, 2017b; Cochran et al., 2018). The second approach, ETAS modeling, also considers event magnitude and time as it predicts the earthquake rate of a stationary Poisson process plus time-decaying aftershocks (Ogata, 1988). The ETAS model assumes a constant stationary seismicity rate which works well for natural (e.g., tectonic) settings but may be a poor fit for regions of induced seismicity that have time-dependent human influences (e.g., oil, gas, geothermal production, fluid injection) (Kothari et al., 2020; Llenos & Michael 2013). Finally, nearest neighbor distance (NND) distributions in the space-time-magnitude domain are indicative of the independent and/or clustered nature of an earthquake sequence or region. For an ETAS distribution, the NND is bimodal with a signal at short rescaled distances indicating clustered behavior, whereas a signal at larger rescaled distances represents independent (Poissonian) behavior (Zaliapin et al., 2008). For NND results in Figures 7-8, the relocated earthquake catalog was used except for the northern basin, where only a small number of events (~280) were accepted for relative relocation (Figure S3d). A comparison between NND results using absolute location and relative relocation for each region can be found in Figure S6.

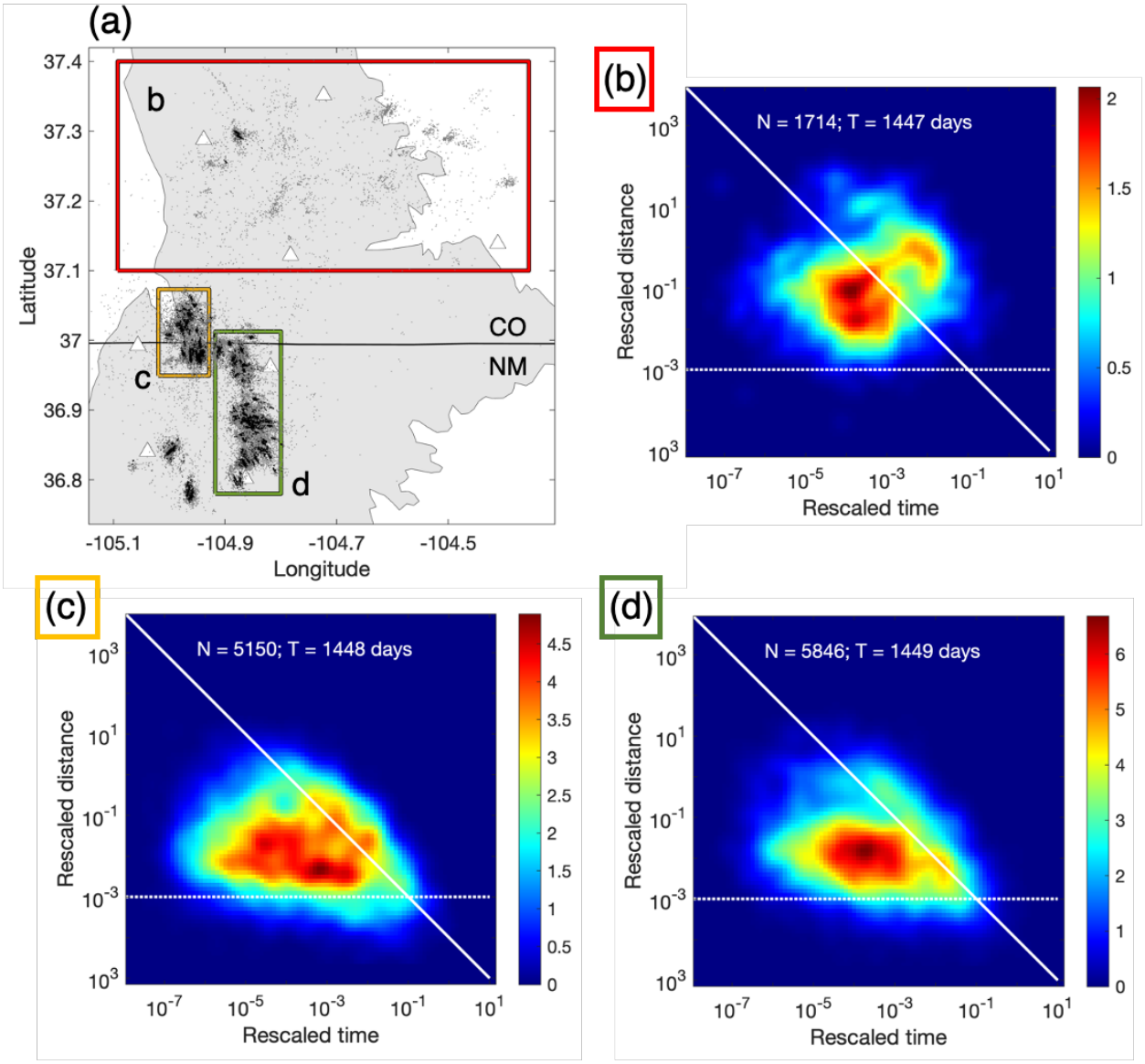

Figure 7. Nearest neighbor time-distance distributions for seismicity in subregions of the Raton Basin. (a) Map of earthquakes and subregions: red for the northern subregion, yellow for the Tercio zone, and green for the Vermejo Park zone. Absolute hypocenters are gray dots and relative hypocenters are black dots. Seismometers are white triangles. (b-d) The nearest neighbor distribution results for each subregion. The labels and colors of each region in (a) correspond to the results in (b-d). Absolute locations were used for the results shown in b and relative relocation results for c-d. The color bar indicates

the number of event pairs at a given rescaled distance-time. The number of earthquakes, N, and the time period, T, is printed on each figure. The diagonal white line represents a stationary behavior. The horizontal white dotted line represents a constant rescaled distance. Consistent lines are used for all NND figures for direct comparisons.

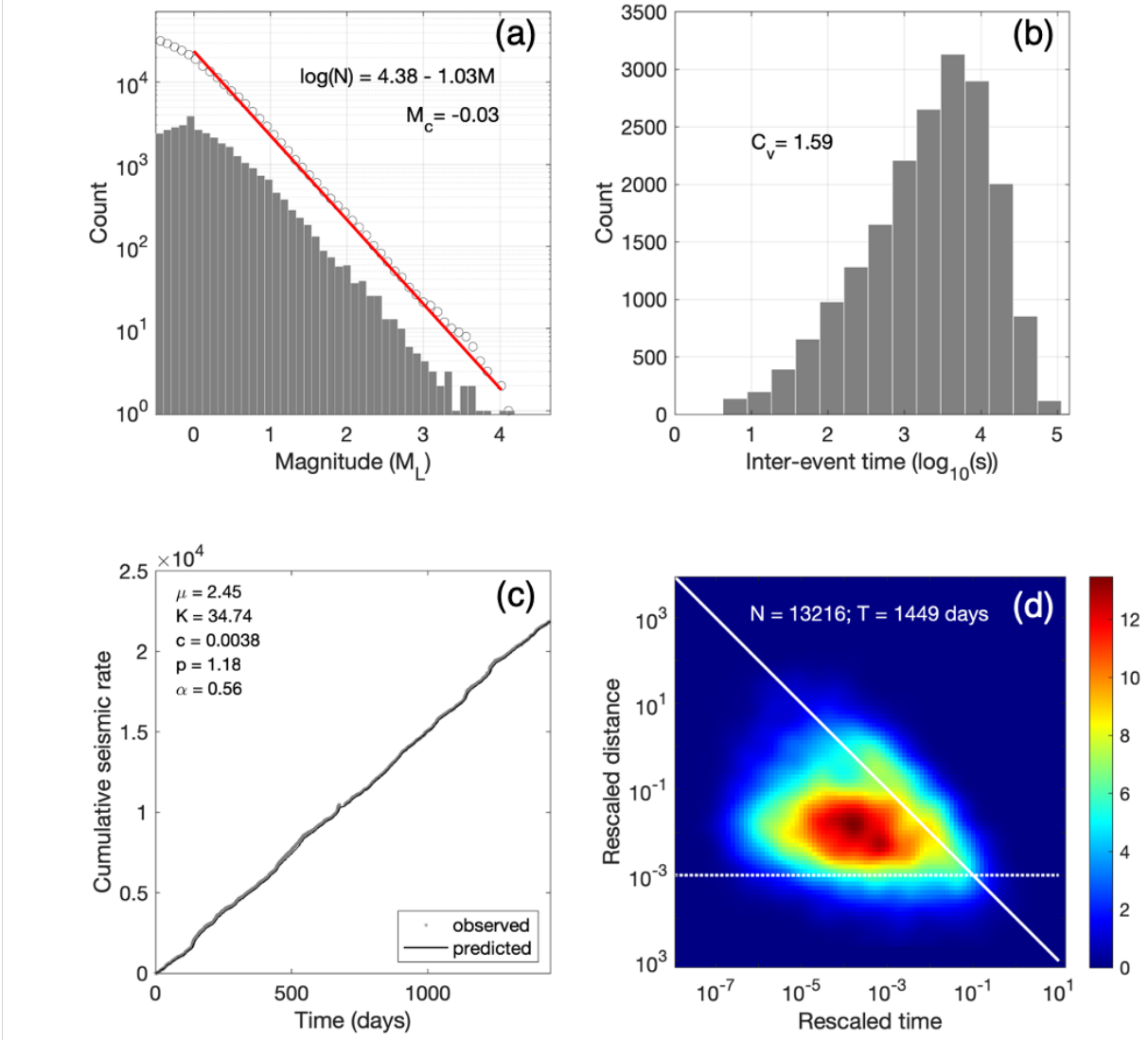

Figure 8. Raton Basin frequency-magnitude and spatiotemporal statistical results. (a) Earthquake frequency-magnitude histogram (gray bars; noncumulative) and cumulative earthquake distribution (gray circles). The red line approximates the best least squares fit to the Gutenberg-Richter relation above the minimum magnitude of completeness (M_c). (b) Inter-event time histograms. The average coefficient of interevent time variation (C_v) is printed. (c) Cumulative number of earthquakes versus the number of days from observed seismicity (gray) and Epidemic Type Aftershock-Sequence (ETAS) modeling (black line). ETAS maximum likelihood parameter estimates are printed (Ogata, 1988). (d) Nearest-neighbor rescaled time-distance distribution. The color bar indicates the number of event pairs at a given rescaled distance-time. The diagonal white line represents a stationary behavior. The horizontal white dotted line represents a constant rescaled distance. Consistent lines are used for all NND figures for direct comparisons.

Results

5.1 Spatial clustering of hypocenters

The majority of hypocenters are tightly clustered in geometries consistent with earthquake activity on unmapped basement faults ~2.5–6 km below sea level (Figure 4c). Absolute hypocenters are heavily concentrated in the central to southern basin with 90% (~34,000 earthquakes) south of 37.05 latitude (Figure 4a). The absolute earthquake locations (Figure 4a, d) collapse into dense elongated clusters after relative relocation (Figure 4b, e). Two of the three previously identified fault zones, the Tercio and Vermejo Park zones (Figure 2, Figure 4), are active during our study period, similar to the 2008-2010 study by Nakai et al. (2017a). Very few earthquakes were detected in the Trinidad zone. Small seismically active zones were identified in the southwest and northwest of the basin by absolute and relocated hypocenters (Figure 4a-b). One of the southwestern clusters was previously identified by Wang et al. (2020) using only one month of nodal data. Absolute hypocenters are sparsely distributed in the remainder of the northern basin, however all but the northwestern group were culled by the relocation criteria.

Application of PCA to the relocated earthquake hypocenters indicates 57 short, <3 km, faults (Figure 5a). The majority of the faults (48 out of 57) strike from approximately WNW to slightly east of north (Figure 5b). WNW-ESE striking faults are the most seismogenic based on the number of events above the M_c. They host ~33% of the total M_L 0.5 earthquakes (Figure 5c).

5.2 Source mechanism constraints

Most focal mechanisms from full moment tensor inversion and first motion picking support the regional scale normal faulting regime (Lund Snee & Zoback, 2020), with a few exceptions showing oblique or reverse regimes (Figure 6). The

strike orientations vary from NE to WNW from north to south. More heterogeneous strikes are observed near the boundary of New Mexico and Colorado (Figure 5-6). In general, the strikes estimated from the PCA analysis (Figure 5) and potential fault planes from focal mechanisms (Figure 6) are comparable in the central to southern basin where most seismicity occurs and the seismograph distribution minimizes azimuthal gaps. Several oblique mechanisms and one reverse faulting mechanism are in the central to southern basin (Figure 6). The reverse event is located in the middle of the Tercio zone. Most other events in the Tercio zone indicate ~NW striking normal faults. Oblique mechanisms are more prevalent near the transition between the Tercio and Vermejo Park zones. Farther south within the middle to southern portion of the Vermejo Park zone most mechanisms indicate WNW to N normal faults (Figure 5-6).

A notable example of inconsistency between the moment tensor and PCA results is found for one fault near the northern edge of the array, ~37.3° N (Figure 6). Its PCA strike estimate is NW and its moment tensor strike estimate is NE (Figure 5a inset & Figure 6). Given the location near the edge of the array the hypocenters may be biased by limited azimuthal coverage. The three-component waveform-based moment tensor estimate of strike is preferred in this location. Additionally, maximum compressive stress indicators near 37.3° N show orientations of ~NNE-NE (Figure 2; Lund Snee & Zoback, 2020), which would be consistent with a ~NE striking normal fault.

5.3 Frequency, magnitude, and temporal clustering statistics

Space-time-magnitude statistics are calculated for the full basin and three subregions: the northern basin, the Tercio zone, and the Vermejo Park zone (Figure 7-8; S3-S6). The M_c varies spatially due to station coverage (Figure S3-S5). Although M_c = -0.13 for the entire catalog (Figure 8a), we conservatively suggest that the catalog is complete to ~M_L 0.5 since this was the maximum M_c of the subregions (Figure S3-S5). However, the following statistical results were all derived using earthquakes with M_L unique to each considered region. The maximum magnitude during our study is M_L 4.2. The b-value for the entire study region is 1.03 (Figure 8a) and the b-values of the three subregions are between 0.98 - 1.06 (Figure S3a-S5a).

Interevent times range from 1-5 s (Figure 8b), similar to the induced seismicity studied by Schoenball and Ellsworth (2017b) in Oklahoma and Southern Kansas. A study of interevent times in south central Kansas by Cochran et al. (2018) finds temporal behavior ranges from

Poissonian (C_v=1) to highly clustered (C_v>7). The full basin C_v is 1.6 (Figure 8b) indicating a small amount of temporal clustering. The C_v of the subregions is slightly higher, ~1.8 for Vermejo Park, ~1.9 for Tercio, and ~2 for the north (Figure S3b-S5b). Cochran et al. (2018) finds earthquake families with C_v<2 are within 10 km of high volume wastewater injection.

ETAS modeling fits the observed seismic rate for the full basin (Figure 8c), as well as the Tercio and Vermejo Park regions (Figure S4-S5). This demonstrates that most of the observed seismicity in the Raton Basin can be modeled by time-independent events and subsequent aftershocks, similar to regions of natural seismicity (Chu et al., 2011). A minor exception is that for the northern subregion, ETAS often underpredicts the seismic rate (Figure S3c) indicating the observed rate has even higher productivity of earthquake-earthquake interactions than predicted by ETAS.

Different NND distributions have been observed for some induced settings compared to tectonic settings (Zaliapin & Ben Zion, 2016). A stronger distribution of independent to clustered seismicity has been found in some induced settings (Zaliapin & Ben Zion, 2016; Cochran et al., 2020). Also, the presence of repeaters, earthquakes that occur at short rescaled distances and long rescaled times, are suggested as an induced seismicity signal (Zaliapin & Ben Zion, 2016). NND distributions for the full basin (Figure 8d) are slightly bimodal with the largest concentration of event pairs at short space-time distances corresponding to clustered seismicity and a smaller distribution along a constant slope corresponding to independent background seismicity. NND distributions for the three subregions (Figure 7c-d) also have a strong clustered behavior and comparatively weak independent behavior. The northern region (Figure 7b) exhibits the clearest separation between the clustered and background mode. However, poorly constrained absolute locations can lead to artifacts at large space-time distances (Zaliapin & Ben-Zion, 2015). A repeater signal may be present for the Vermejo Park zone appearing as a lobe in the bottom right of Figure 7d, but it is not apparent for the other considered regions (Figure 8d, Figure 7b-c).

Discussion

6.1 Basement fault systems beneath the Raton Basin

The spatial distribution of seismicity in the new catalog provides evidence for local variability of fault orientations that is not apparent in prior work using the TA or short-term aftershock deployments (Rubinstein et al., 2014; Nakai et al., 2017b; Barnhart et al., 2014). Prior work indicated primarily N to NNE striking normal faulting earthquakes (Rubinstein et al., 2014; Barnhart et al., 2014; Nakai et al., 2017b), which were grouped into three zones of seismicity ~10-20 km in length: the Trinidad, Vermejo Park, and Tercio zones (Figure 2). During 2016-2020, the Vermejo Park and Tercio zones were much more active than the Trinidad zone, whose activity has greatly diminished since hosting a M_W 5.3 event in 2011 and continued to diminish during 2016-2020 (Figure 9e). Primarily using TA data with ~70-km station spacing, Nakai et al. (2017b) suggested that the Vermejo Park and Tercio zones were long (~10-20 km) N-S normal faults. With the local array catalog from 2016 to 2020, we find 57 shorter faults across the Raton Basin with variable strikes (Figure 5) and faulting regimes (Figure 6). Most of these short faults are concentrated in the Vermejo Park and Tercio zones,

where discrete faults with lengths of ~1-3 km combine to form the previously identified broader zones of seismicity. The nearly contiguous seismicity between the Tercio and Vermejo Park zones suggests their activity may be linked. These multi-scale fault zone structures are similar to but more extensive than earlier suggestions of en echelon faults within the Trinidad zone near the time of the 2011 M_W 5.3 earthquake sequence (Rubinstein et al., 2014).

A potential implication of the multi-scale fault zone structure is that the maximum potential earthquake magnitude may be smaller if there are no continuous faults that span the ~20 km long Vermejo Park zone or ~10 km long Tercio zone. However, ruptures may span multiple nearby fault segments (e.g., Landers earthquake, Li et al., 1994; and Hector Mine earthquake, Treiman et al., 2002) such that the maximum fault length is not a reliable predictor of the maximum earthquake magnitude. Such co-slipping of en-echelon fault systems has been observed from induced seismicity in Alberta, Canada (M_W 4.1, Wang et al., 2017). Within the Raton Basin, the largest earthquake since injection began is the M_W 5.3 Trinidad event with a geodetically estimated rupture length of ~8-10 km (Barnhart et al., 2014), which is shorter than the ~14 km total length of the Trinidad zone of seismicity (Rubinstein et al., 2014; Meremonte et al., 2002). A local seismic network was not in place prior to the M_W 5.3 event therefore it is unclear whether it ruptured one fault or multiple shorter faults, but the aftershock locations suggest the presence of multiple segments with strikes rotated closer to North, instead of the orientation of the composite Trinidad zone of seismicity (Figure 9a; Rubinstein et al., 2014).

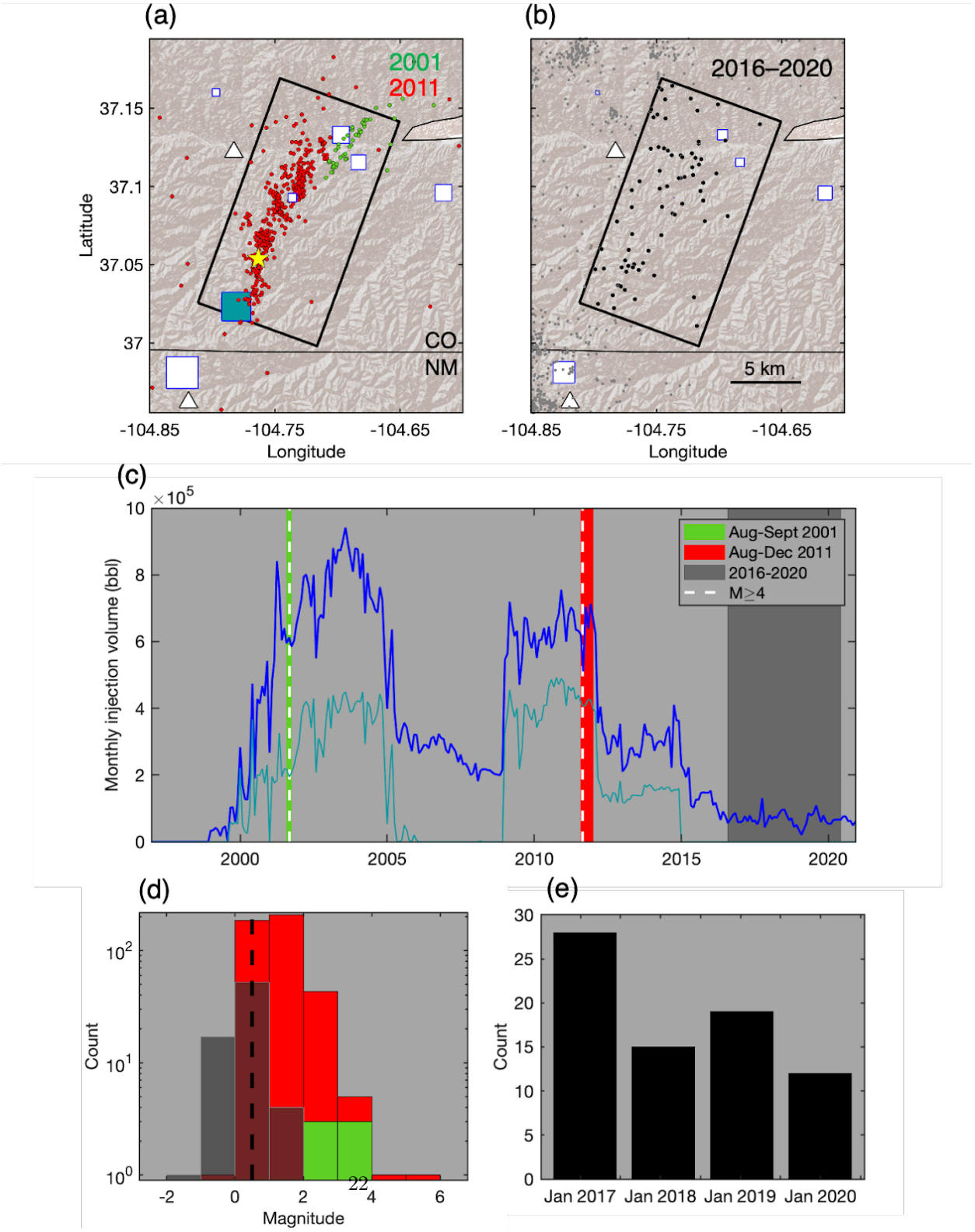
(a)
2001
2011
37.15
37.1
37.05
37
Latitude
CO
NM
-104.85
-104.75
-104.65
Longitude
(b)
2016–2020
5 km
-104.85
-104.75
-104.65
Longitude
(c)
×10^5
10
8
6
4
2
0
Monthly injection volume (bbl)
Aug-Sept 2001
Aug-Dec 2011
2016-2020
M≥4
2000
2005
2010
2015
2020
(d)
10^2
10^1
10^0
Count
-2
0
2
4
6
Magnitude
(e)
30
25
20
15
10
5
0
Count
Jan 2017
Jan 2018
Jan 2019
Jan 2020

Figure 9. Evolution of Trinidad zone seismicity. (**a-b**) Maps of earthquakes in the Trinidad zone (black box) from (**a**) Aug–Dec 2001 (green, Meremonte et al., 2002), Aug–Dec 2011 (red; Rubinstein et al., 2014) and (**b**) our July 2016–July 2020 catalog (black and gray). Seismometers are white triangles. Wastewater injection wells are squares and are scaled by average injection volume from 2008-2012 for (a) and from 2016 to 2020 for (b). The yellow star is the 2011 M_w 5.3 earthquake. (**c**) Total monthly wastewater injection volume within the Trinidad zone shown in dark blue. Turquoise monthly wastewater injection volume is for two collocated wells shown as a turquoise well in (a). Shaded regions indicate times of earthquake studies, see legend. White dashed lines are M 4 earthquakes from the USGS catalog within 10 km of the Trinidad zone. (**d**) Earthquake magnitudes for each catalog within the Trinidad zone. Legend colors from (c) apply to (d). Black dashed line marks the minimum magnitude of completeness for our 2016-2020 catalog. (**e**) Number of earthquakes per year within Trinidad zone for our catalog shown in (b).

The changes in fault orientation (Figure 5) and evidence of different slip regimes (Figure 6), specifically along the CO-NM border, indicate either stress conditions that change over short-length scales (~5-10 km) or stress perturbations that are sufficient to reactivate non-optimally oriented faults. A stress rotation from N-S maximum horizontal stress in the mid to northern basin to E-W at the southeastern edge (Figure 2) may help explain the variable strikes (Lund Snee & Zoback, 2020; Wang et al., 2020) but there are no stress measurements to compare to the most seismically active parts of the central to southern basin. Alternatively, the regional stress field may be modified by local stresses or earthquakes may occur on non-optimally oriented faults, as observed in some areas of fluid injection. Such stress perturbations are often observed from high-rate injections like hydraulic fracturing (e.g., Shen et al., 2021) or geothermal exploitations (e.g., Martinez-Garzon et al., 2016). At maximum injection pressures for the Geysers geothermal field, a range of fault orientations are activated including non-optimally oriented faults at maximum injection pressure (Martinez-Garzon et al., 2016). We generally observe more variable fault orientations closer to wastewater injection wells (e.g., the CO-NM border, Figure 5a). Non-optimally oriented faults in Oklahoma and Kansas are suggested to reactivate from either high pore pressure increase or potentially static stress changes from nearby seismogenic faults (Qin et al., 2019; Amemoutou et al., 2021). A finer resolution of the wastewater injection record is necessary for a comparison between fault orientations, injection rate changes, and static stress changes.

6.2 Evolution of wastewater injection and seismicity

6.2.1 Full basin summary The seismogenic faults from this study are located in the basement similar to previous studies of Raton Basin seismicity (Nakai et al., 2017b; Rubinstein et al., 2014) as well as Oklahoma and Kansas (Schoenball & Ellsworth 2017a; Qin et al., 2019). Permeable pathways, such as faults, provide a potential link between shallow wastewater injection and re-

activation of basement faults under the Raton Basin (Nakai et al., 2017b). In the Raton Basin mapped faults and intrusions are observed at the surface and basement faults are inferred from earthquake locations but there are no direct observations of permeable pathways that connect the injection reservoir to the basement. However, mantle-derived helium often found in geothermal springs along faults at locations near the Raton Basin, e.g., Sheep Mountain and Bravo Dome, suggests that permeable connections between mantle depths and Earth's surface are common in this region of the southern Rocky Mountains (Karlstrom et al., 2013).

To understand the evolution of wastewater injection, we examine the average monthly injection for three four-year time periods in the Raton Basin (Figure 10). The wastewater injection record by well is complete from 2006-2020. Similar to Weingarten et al., (2015), we consider injection 300,000 bbl/month as high-rate, <100,000 bbl/month as low-rate, and rates between as moderate. The injection rate and total injection volume in the Raton Basin decreases chronologically from 2008 to 2020 (Figure 10a-c). The number of high-rate injection wells decreased from two during 2008-2012 to zero from 2012-2020 (Figure 10). Injection rate declined in the south and central basin from 2008-2020 and is more evenly distributed across the basin by 2016-2020 (Figure 10). The northernmost well and two wells just south of the state border remain high- to moderate-rate injectors during all considered time periods. During our earthquake catalog from 2016 to 2020, these three wells operate at >170,000 bbl/month and in total 6 wells are moderate-rate injectors. Similar injection rates, >150,000 bbl/month, were reported for all wells associated with induced seismicity for the Barnett Shale in Texas with some wells operating at this rate aseismically (Frohlich, 2012).

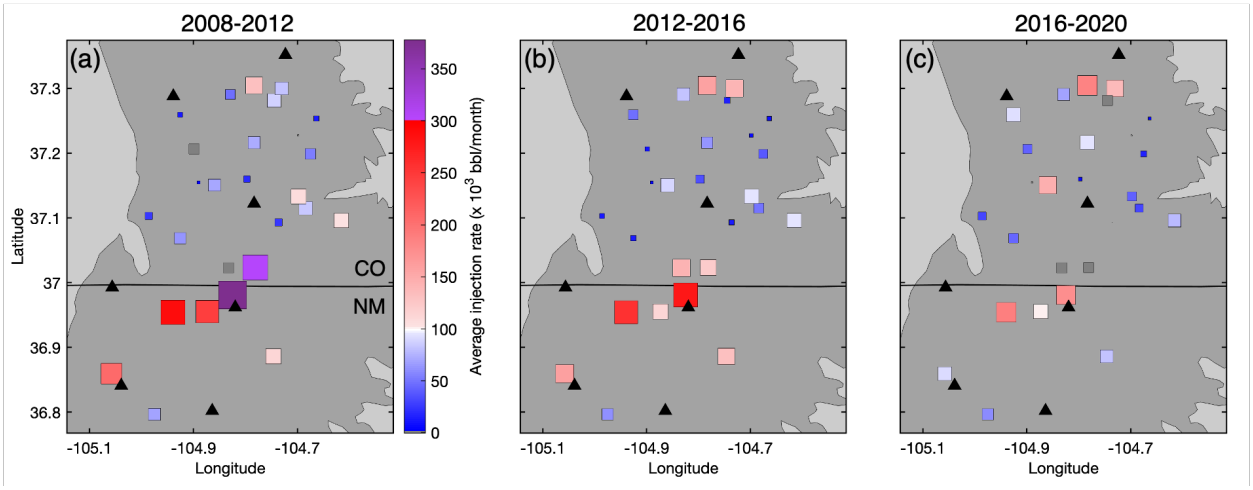

Figure 10. The average monthly wastewater injection volume during three time periods indicated by the titles for a-c. The color bar from (a) can be used for (b-

c). Purple indicates high-rate, red indicates moderate-rate, and blue indicates low-rate injection wells. Squares scale with the average injection volume and are consistent between figures. Gray squares indicate wells with no reported injection volume. Black triangles are seismometers.

Greater than 90% of earthquakes occur less than 10 km from the nearest wastewater disposal well from 2016 to 2020 (Figure 11) with an average earthquake to well distance of 5.8 km. Given the proximity of seismicity to injection wells, pore fluid pressure increases are a likely driver of fault reactivation. Previously modeled pore fluid pressure increases of 0.08 MPa in the Vermejo Park zone are sufficient to trigger earthquakes (Nakai et al., 2017b). The timing of pore fluid pressure changes is strongly dependent on hydraulic diffusivity (Barbour et al., 2017), which may explain the lack of a short-term (time scales less than years) temporal correlation between wastewater injection and seismicity (Figure 1a; Figure S7). The cumulative injection rate was steady to slightly decreasing from 2016 to 2020 and no apparent correlation exists between the cumulative injection volume and seismicity (Figure S7). The temporal evolution in the Raton Basin is similar to other areas where induced seismicity can lag several years behind the initiation of wastewater disposal (Schoenball et al., 2018). Poroelastic stresses may also contribute to inducing seismicity and could play a greater role in triggering far-field earthquakes (Goebel et al., 2017) like those >20 km from wastewater injection (Figure 11).

6.2.2 Tercio and Vermejo Park zones From 2008–2020, the wells with the highest injection rates, largest cumulative injection volume, and most continuous injection history lie within the Tercio and Vermejo Park zones just south of the CO-NM border (Figure 10). These zones are the most seismically active during this study (Figure 11). Two additional wells (VPR 007 and VPR 042) are co-located between the large injectors. All four wells are within ~10 km horizontal distance and <250 m vertical distance. They cumulatively inject >450,000 bbl/month on average from 2016 to 2020. Weingarten et al. (2015) found that the likelihood a wastewater injection well is associated with earthquakes increases as the maximum injection rate increases, e.g., high-rate wells are twice as likely to be associated with earthquakes as low-rate wells. High-rate wells perturb pressure at larger magnitude and further extent than low-rate wells (Weingarten et al., 2015). The larger spatial effect of high-rate wells also increases the probability of encountering faults. Absolute earthquake locations extend from the area of large cumulative injection along the border to 15 km north in the Tercio zone and 20 km south in the Vermejo Park zone (Figure 11c). At the furthest extents in these zones, earthquakes are closer to other injection wells but are not spatially contiguous with these wells.

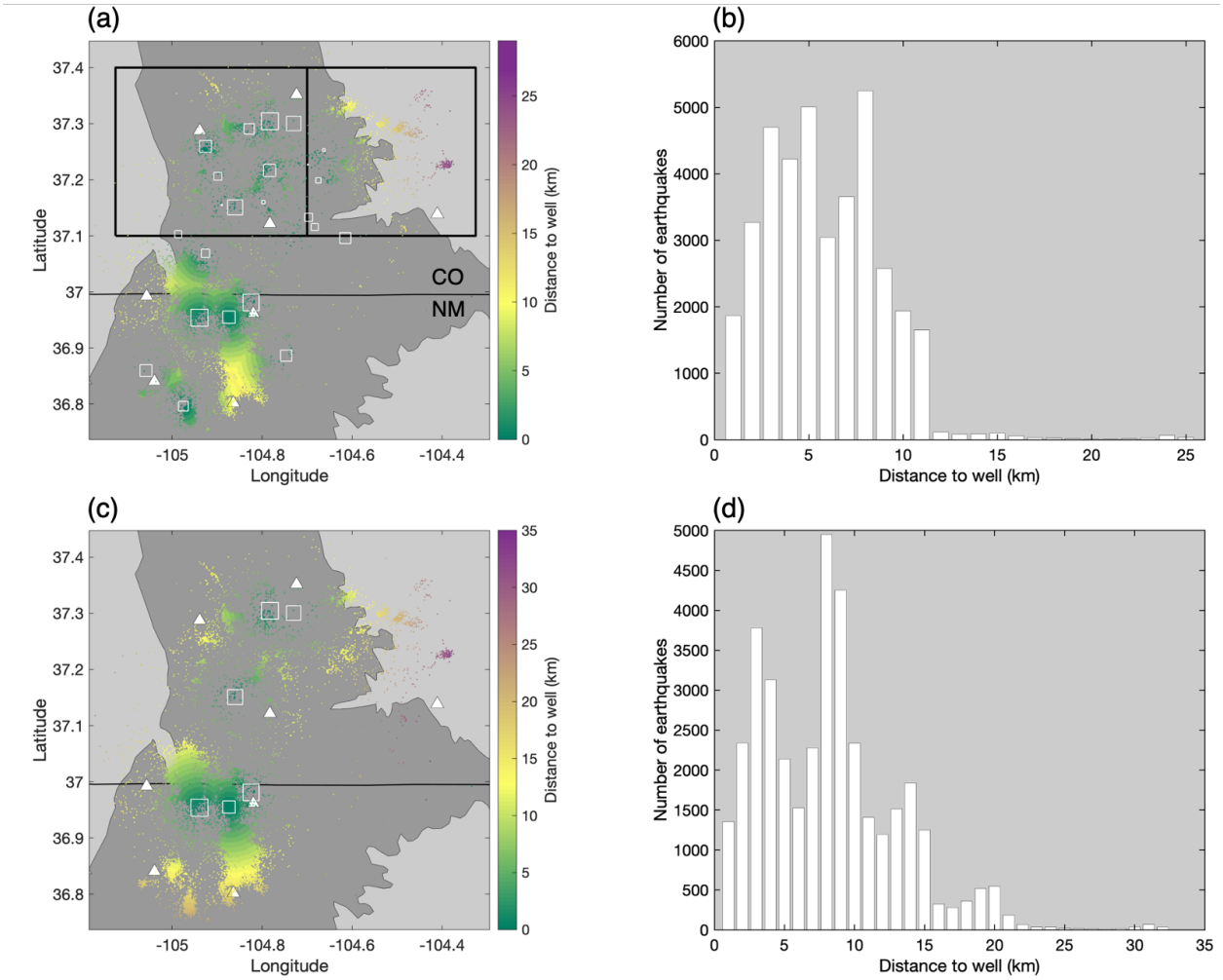

Figure 11. Earthquake distance to nearest wastewater injection well. Map of earthquake distance to (a) the nearest wastewater injection well and (c) the nearest moderate-rate injection well. Color corresponds to distance. The size of white squares scale with the average monthly injection volume from 2016 to 2020. White triangles are seismometers. The perimeter of the black box in (a) is to distinguish the north mentioned in 6.2.3 and the line separates the northeast and northwest. (b) Distribution of distances from (a). (d) Distribution of distances from (c).

6.2.3 Northeastern basin Seismicity is observed at the greatest distance from wells beyond the northeastern margin of the basin. Earthquakes occur up to ~27 km from the nearest injection well and ~35 km from the nearest moderate-rate well (Figure 11). In Oklahoma, induced earthquakes have oc-

curred 20-40 km from injection wells (Keranen et al., 2014; Goebel et al., 2017). Above basement injection, as is the case in the Raton Basin, has been linked to larger spatial footprints of seismicity in a global compilation (Goebel & Brodsky, 2018). Assessing the origin of the more distant events is difficult because catalog sensitivity to M<3 earthquakes is sporadic over the past two decades. The earthquake catalog by Nakai et al. (2017) from 2008-2010, has 70 earthquakes per year in the north and 23 in the northeast above their M_c of 1.3 (see Figure 11a for definition of north and northeast). Using the same M_c, we find a comparable number of earthquakes in the north, 63 earthquakes/year, and sixty percent more earthquakes in the northeast, 37 earthquakes/year. Injection rates in the northern basin have not changed dramatically over time (Figure 10). It is plausible that seismicity is extending farther northeast from wells after two decades of pore-pressure diffusion, however poroelastic effects may become more influential at greater distance from wells (Goebel et al., 2017). Reanalysis of earlier seismic data and further hydrogeologic modeling (e.g., Nakai et al., 2017b) are needed to test potential linkages between the northeastern extent of earthquake activity and wastewater injection at distances >25 km.

6.2.4 Trinidad zone Few earthquakes are observed in the Trinidad zone which hosted the largest recorded earthquake in the basin (M_W 5.3) in the second of two short-lived earthquake sequences in 2001 and 2011 (Figure 9, Meremonte et al. 2002; Rubinstein et al., 2014). Approximately seventy earthquakes with M_L<2 are located in the Trindad zone during our study (Figure 9b) with none surviving the relocation step (Figure 4b). The earthquake rate decreases from the beginning to end of our study (Figure 9e). Only one earthquake was located in the Trindad zone for the 2008–2010 earthquake catalog with M_c=1.3 by Nakai et al. (2017b). The combination of results suggests that seismicity in the Trinidad zone is episodic, capable of quick bursts of activity and quiescent periods on the order of years.

The monthly injection rate in the Trinidad zone for the years preceding the 2011 sequence was ~600,000 bbl/month (Figure 9c), ~70-80% of which was contributed by the two collocated high-rate wells nearest the M_W 5.3 earthquake (Figure 9a & c). In 2012 the rate dropped to ~300,000 bbl/month and by 2016 to ~100,000 bbl/month. The two co-located wells were completely shut-in by January 2015, ~20 months prior to our study (Figure 9c).

We suggest the significant decrease in wastewater injection, specifically the shut-in of the highest-rate injection wells, led to the low and declining seismicity in the Trinidad zone from 2016 to 2020. Well shut-in has been used as a mitigating step following large earthquakes as it can reduce the earthquake rate in some regions at least on short time- and length- scales (e.g., Pawnee and Cushing earthquakes). Goebel et al. (2019) found fluid pressures can decrease within the injection reservoir at kilometer-length scales within days of well shut-in. In our case, there was no large event that preceded well shut-in in January 2015. We speculate that fluid pressure decreased sufficiently in the twenty months follow-

ing the complete shut-in of two wells and general decrease in overall wastewater injection to result in our observation of low seismic activity (Figure 9); poroelastic effect could be less effective. The Trinidad zone may be a useful example for further studying the evolution of seismicity following cessation of about a decade of injection during which moderate magnitude events occurred.

6.3 Statistical similarity to tectonic sequences

Induced and tectonic settings are suggested to have different spatiotemporal-magnitude and frequency-magnitude statistics since the physical mechanisms driving the processes are different. The b-value for the Raton Basin is ~1, which is expected for tectonic seismicity but has also been found for induced settings (e.g., Cochran et al., 2020; Wang et al., 2020). In cases of clear anthropogenic forcing, such as geothermal stimulation, independent earthquakes dominate the spatiotemporal-magnitude behavior (Schoenball et al., 2015; Martinez-Garzon et al., 2018). In regions of tectonic earthquakes, less independent and more clustered earthquakes are observed compared to induced settings (Zaliapin & Ben Zion, 2016). The C_v, ETAS modeling, and NND distribution of the Raton Basin all indicate clustered behavior, varying from moderate to high depending on the considered subregion and method (Figure 7, 8, S3-S5).

The dominance of the clustered mode at 10^{-2} rescaled distance and 10^{-4} rescaled time in Figure 8d is similar to the results for the induced setting of southern Kansas and Oklahoma (Schoenball & Ellsworth, 2017b; Verdecchia et al., 2021) and the mixed (induced and tectonic) setting of the Salton Sea geothermal area (Zaliapin & Ben Zion, 2016). In addition to the type of seismicity (e.g., induced, tectonic), geologic setting is suggested to affect the spatiotemporal-magnitude statistics (Martinez-Garzon et al., 2018; Vasylkivska & Huerta, 2017). The higher structural complexity of the Salton Sea geothermal field has been proposed as a reason for its different response to fluid injection compared to other regions like Coso and the Geysers (Martinez-Garzon et al., 2018).

The strong clustered behavior of the Raton Basin suggests earthquake-earthquake interactions are more significant than independent sequences, such as earthquake-fluid interactions. Similar results in a study by Schoenball et al. (2017b) led to the conclusion that earthquake sequences in Oklahoma and southern Kansas are initiated by anthropogenic stressing but stored tectonic energy drives sequences. Alternatively, a one-month study by Cochran et al. (2020) found independent sequences dominate Oklahoma seismicity and suggests they are directly driven by high stressing rates of wastewater disposal wells. Wastewater injection rates in their study region were 7-8 million bbl/month, ~4-5 times the wastewater injection rate during our study (Figure 1b). For the Raton Basin we suggest, similar to Schoenball et al., (2017b), that small changes in pore fluid pressure from moderate- to low-rate wastewater injection decreases the frictional resistance on faults, permitting the stored tectonic stress to initiate slip and continue through interevent triggering (earthquake-earthquake interactions).

7. Conclusions

A four-year earthquake catalog of ~38,000 earthquakes aids in identifying the seismogenic structures of the Raton Basin and characterizing the spatiotemporal statistical earthquake behavior. Additionally, the catalog is compared to the wastewater injection record. Sixty short, 1-3 km, faults with a range of strikes from WNW to NNE are active in the basement beneath the Raton Basin. The majority of fault motion agrees with the regional scale normal faulting regime while some oblique and reverse slip exists.

The Trinidad and Vermejo Park zones host over 80% of the basin's seismicity. The Trinidad zone that hosted the 2011 M_w 5.3 earthquake experienced seismic quiescence from 2016 to 2020, likely associated with the large decrease in the wastewater injection rate in 2015. Unlike some regions of induced seismicity with distinct independent clusters reflecting strong fluid-earthquake interactions, the spatiotemporal-magnitude behavior of the seismicity in the Raton Basin is more strongly clustered, similar to tectonic regions. We suggest that the low- to moderate-rate wastewater injection of the Raton Basin may only initiate earthquake sequences by decreasing the frictional resistance on faults whereas stored tectonic stress is responsible for subsequent earthquake-earthquake interactions.

Acknowledgements and Data Availability

Waveform data and metadata used in this study are publicly available through the Incorporated Research Institutions for Seismology Data Management Center (IRIS DMC) using the network and station information in Table S1 (http://ds.iris.edu/ds/nodes/dmc/). The IRIS DMC is supported by the National Science Foundation under Cooperative Support Agreement EAR-1851048. The Raton Basin earthquake catalog from 2016 to 2020 is available at the ISC bulletin (http://www.isc.ac.uk/iscbulletin/search/catalogue/) upon publication. Figures were produced using MATLAB and GMT (Wessel & Smith, 1991). We thank Matt Weingarten, Justin Rubinstein, and Jenny Nakai for constructive discussions. Private landowners, including the Vermejo Park Ranch, generously hosted seismometers. We thank all the fieldworkers who contributed to the broadband and node arrays used in the study. This research was supported by NSF EAR 1554908.

References

Allen, R. V. (1978). Automatic earthquake recognition and timing from single traces. *Bull. seism.* Soc. Am., 68(5), 1521–1532.

Amemoutou, A., Martínez-Garzón, P., Kwiatek, G., Rubinstein, J., & Bohnhoff, M. (2021). Earthquake Source Mechanisms and Stress Field Variations Associated with Wastewater Induced Seismicity in Southern Kansas, USA. *Journal of*

Geophysical Research: Solid Earth, 126, e2020JB021625. https://doi.org/10.1029/2020JB021625

ANSS ComCat (2021). Advanced National Seismic System Comprehensive Earthquake Catalog. Retrieved from https://earthquake.usgs.gov/data/comcat/. (Accessed Feb 2021).

Baltz E.H. (1965). Stratigraphy and history of the Raton basin and notes on San Luis basin, Colorado-New Mexico. *American Association of Petroleum Geologists Bulletin, v. 49*, 2041-2075.

Barbour, A. J., Norbeck, J. H., & Rubinstein, J. L. (2017). The effects of varying injection rates in Osage County, Oklahoma, on the 2016 Mw 5.8 Pawnee earthquake. *Seismological Research Letters, 88(4)*, 1040. https://doi.org/10.1785/0220170003

Barnhart, W. D., Benz, H. M., Hayes, G. P., Rubinstein, J. L., & Bergman, E. (2014), Seismological and geodetic constraints on the 2011 Mw5.3 Trinidad, Colorado earthquake and induced deformation in the Raton Basin, *J. Geophys. Res. Solid Earth, 119*, 7923–7933, doi:10.1002/ 2014JB011227.

Blackwell, D. D., Richards, M. C., Frone, Z. S., Batir, J. F., Williams, M. A., Ruzo, A. A., & Dingwall, R. K., (2011). SMU Geothermal Laboratory Heat Flow Map of the Conterminous United States, 2011. Retrieved from http://www.smu.edu/geothermal

Chu, A., Schoenberg, F. P., Bird, P., Jackson, D. D. & Kagan, Y. Y. (2011). Comparison of ETAS parameter estimates across different global tectonic zones, *Bull. seism. Soc. Am., 101(5)*, 2323–2339.

Cochran, E. S., Ross, Z. E., Harrington, R. M., Dougherty, S. L., & Rubinstein, J. L. (2018). Induced earthquake families reveal distinctive evolutionary patterns near disposal wells. *Journal of Geophysical Research: Solid Earth*, *123*, 8045–8055. https://doi.org/10.1029/2018JB016270.

Cochran, E. S., Wickham-Piotrowski, A., Kemna, K., Harington, R., Dougherty, S., & Castro, A. P., (2020). Minimal clustering of injection-induced earthquakes observed with a large-n seismic array. *Bulletin of the Seismological Society of America, 110(5)*, 2005-2017. https://doi.org/10.1785/0120200101.

COGCC (2021). Colorado Oil and Gas Conservation Commission. Retrieved from http://cogcc.state.co.us/data.html#/cogis. (Accessed Feb 2021).

Dreger, D. S. (2003). TDMT_INV: Time domain seismic moment tensor inversion. In W. H. K. Lee et al., (eds.), *International Handbook of Earthquake and Engineering Seismology, Part B, Int. Geophys. Ser (Vol. 81*, p. 1627). New York: Academic Press.

Earle, P. S., & Shearer, P. M. (1994). Characterization of global seismograms using an automatic-picking algorithm. *Bull. Seismol. Soc. Am., 84(2)*, 366–376.

Edwards C.L., Reiter M., Shearer C., & Young, W. (1978). Terrestrial heat flow and crustal radioactivity in northeastern New Mexico and southeastern Colorado. *Geol. Soc. Am. Bull., 89*, pp. 1341-1350

Ellsworth, W. L. (2013). Injection-induced earthquakes. *Science, 341(6142)*, 1225942. https://doi.org/10.1126/science.1225942

Farrell, S., Husen, & Smith, R.B. (2009). Earthquake swarm and b-value characterization of the Yellowstone volcano-tectonic system. *J. Volcanol. Geotherm. Res.188*, 260–276.

Frohlich, C., Hayward, C., Rosenblit, J., Aiken, C., Hennings, P., Savvaidis, A., ... & DeShon, H. R. (2020). Onset and cause of increased seismic activity near Pecos, West Texas, United States, from observations at the Lajitas TXAR Seismic Array. *Journal of Geophysical Research: Solid Earth*, *125*(1), e2019JB017737.

Frohlich, C. (2012). Two-year survey comparing earthquake activity and injection-well locations in the Barnett Shale, Texas. *Proceedings of the National Academy of Sciences, 109*, 35, 13934-13938

Goebel, T. H., & Brodsky, E. E. (2018). The spatial footprint of injection wells in a global compilation of induced earthquake sequences. *Science*, *361(6405)*, 899-904.

Goebel, T. H., Weingarten, M., Chen, X., Haffener, J., & Brodsky, E. E. (2017). The 2016 Mw5.1 Fairview, Oklahoma earthquakes: Evidence for long-range poroelastic triggering at >40 km from fluid disposal wells. Earth and Planetary Science Letters, 472, 50–61. https://doi.org/10.1016/j.epsl.2017.05.011

Goebel, T. H. W., Hosseini, S. M., Cappa, F., Hauksson, E., Ampuero, J. P., Aminzadeh, F., & Saleeby, J. B. (2016). Wastewater disposal and earthquake swarm activity at the southern end of the Central Valley, California. *Geophysical Research Letters, 43*, 1–8. https://doi.org/10.1002/2015GL066948

Goebel, T. H. W., Rosson, Z., Brodsky, E. E., & Walter, J. I. (2019). Aftershock deficiency of induced earthquake sequences during rapid mitigation efforts in Oklahoma. *Earth and Planetary Science Letters, 522*, 135–143. https://doi.org/10.1016/j.epsl.2019.06.036

Gutenberg, B., & Richter, C. F. (1956). Earthquake magnitude, intensity, energy, and acceleration. *Bull. Seismol. Soc. Am. 46*, 105–145.

Healy, J. H., Rubey, W. W., Griggs, D. T., & Raleigh, C. B. (1968). The Denver earthquakes. *Science 161 (3848)*, 1301–10.

Hills, R. C. (1899). Description of the Elmoro quadrangle, Colorado, U.S. *Geol. Survey Geol. Atlas, Folio 58*, 6.

Hincks, T., Aspinall, W., Cooke, R., & Gernon, T. (2018). Oklahoma's induced seismicity strongly linked to wastewater injection depth. *Science*, *359*, 1251–1255.

Johnson, R. G., & Wood, H. H., Jr. (1956). Stratigraphy of upper Cretaceous and Tertiary rocks of Raton Basin, Colorado and New Mexico. *American Association of Petroleum Geologists Bulletin, V. 40*, p. 707-721.

Johnson, R. G., & Finn, T. M. (2001). Potential for a Basin-Centered Gas Accumulation in the Raton Basin, Colorado and New Mexico. *USGS Bulletin,* 2184-B.

Karlstrom, K. E., Crossey, L. J., Hilton, D. R., and Barry, P. H. (2013). Mantle He-3 and CO_2 degassing in carbonic and geothermal springs of Colorado and implications for neotectonics of the Rocky Mountains. *Geology, 41*, pp. 495-498

Keranen, K. M., & Weingarten, M. (2018). Induced seismicity. *Annual Review of Earth and Planetary Sciences, 46(1)*, 149–174. https://doi.org/10.1146/annurev-earth-082517-010054

Keranen, K. M., Weingarten, M., Abers, G. A., Bekins, B. A., & Ge, S. (2014). Sharp increase in central Oklahoma seismicity since 2008 induced by massive wastewater injection. *Science, 345(6195)*, 448-451.

Kissling, E., Ellsworth, W., Eberhart-Phillips, D. and Kradolfer, E. (1994). Initial reference models in local earthquake tomography. *J. Geophys. Res., 99*, 19635–19646.

Kothari, S., Shcherbakov, R., & Atkinson, G. (2020). Statistical modeling and characterization of induced seismicity within the Western Canada Sedimentary Basin. *Journal of Geophysical Research: Solid Earth, 125*, e2020JB020606. https://doi.org/ 10.1029/2020JB020606

Langenbruch, C., Weingarten, M. & Zoback, M. D. (2018). Physics-based forecasting of man-made earthquake hazards in Oklahoma and Kansas. *Nat. Commun. 9*, 3946.

Li Y. G., Vidale J. E., Aki K., & Marone, C. J. (1994). Fine structure of the Landers fault zone: segmentation and the rupture process. *Science, 265*, 367.

Liu, M., Zhang, M., Zhu, W., Ellsworth, W. L., & Li, H. (2020). Rapid characterization of the July 2019 Ridgecrest, California, earthquake sequence from raw seismic data using machine learning phase picker. *Geophysical Research Letters, 47*, e2019GL086189. https:/ /doi.org/10.1029/2019GL086189

Llenos, A. L., & Michael, A. J., (2013). Modeling earthquake rate changes in Oklahoma and Arkansas: possible Signatures of induced seismicity. *Bull. Seismol. Soc. Am. 103*, 2850–2861. http://dx.doi.org/10.1785/0120130017

Martínez-Garzón, P., Kwiatek, G., Bohnhoff, M., & Dresen, G. (2016). Impact of fluid injection on fracture reactivation at The Geysers geothermal field. *J. Geophys. Res. Solid Earth, 121*, 7432–7449, doi:10.1002/2016JB013137

Martínez-Garzón, P., Zaliapin, I., Ben-Zion, Y., Kwiatek, G., & Bohnhoff, M. (2018). Comparative study of earthquake clustering in relation to hydraulic activities at geothermal fields in California. *Journal of Geophysical Research: Solid Earth, 123*, 4041–4062. https://doi.org/10.1029/2017JB014972

McGarr, A. (2014). Maximum magnitude earthquakes induced by fluid injection. *Journal of Geophysical Research: solid earth*, *119*(2), 1008-1019.

Meremonte, M. E., J. C. Lahr, A. D. Frankel, J. W. Dewey, A. J. Crone, D. E. Overturf, D. L. Carver, & W. T. Bice (2002). Investigation of an earthquake swarm near Trinidad, Colorado, August–October 2001, U.S. Geol. Surv. Open-File Rept. 02-0073.

Mousavi, S. M., Ogwari, P. O., Horton, S. P., & Langston, C. A. (2017). Spatio-temporal evolution of frequency-magnitude distribution and seismogenic index during initiation of induced seismicity at Guy-Greenbrier, Arkansas. *Physics of the Earth and Planetary Interiors, 267*, 53–66. https://doi.org/10.1016/j.pepi.2017.04.005

Nakai, J. S., Sheehan, A. F., & Bilek, S. L. (2017a). Seismicity of the Rocky Mountains and Rio Grande Rift from the EarthScope Transportable Array and CREST temporary seismic networks, 2008–2010. *Journal of Geophysical Research: Earth Surface, 122*, 2173–2192. https://doi.org/ 10.1002/2016JB013389

Nakai, J. S., Weingarten, M., Sheehan, A. F., Bilek, S. L., & Ge, S. (2017b). A possible causative mechanism of Raton Basin, New Mexico and Colorado earthquakes using recent seismicity patterns and pore pressure modeling. *Journal of Geophysical Research: Solid Earth, 122(10)*, 8051-8065.

NMOCD (2021). New Mexico Oil and Conservation Division. Retrieved from https://wwwapps.emnrd.state.nm.us/ocd/ocdpermitting/Data/Wells.aspx. (Accessed Feb 2021)

Ogata, Y. (1988). Statistical models for earthquake occurrences and residual analysis for point processes. *Journal of the American Statistical Association, 83(401)*, 9–27. https://doi.org/10.1080/01621459.1988.10478560

Park, Y., Mousavi, S. M., Zhu, W., Ellsworth, W. L., & Beroza, G. C. (2020). Machine learning-based analysis of the Guy-Greenbrier, Arkansas earthquakes: A tale of two sequences. *Geophysical Research Letters, 47*, e2020GL087032. https:// doi.org/10.1029/2020GL087032

Papadopulous, S. S., & Associates, Inc. (2008). Coalbed Methane Stream Depletion Assessment Study- Raton Basin, Colorado. In conjunction with: Colorado Geological Survey, Denver, Colorado.

Qin, Y., Chen, X., Walter, J. I., Haffener, J., Trugman, D. T., Carpenter, B. M., et al. (2019). Deciphering the stress state of seismogenic faults in Oklahoma and southern Kansas based on an improved stress map. *Journal Geophysical Research: Solid Earth, 124*, 12,920–12,934. https://doi.org/ 10.1029/2019JB018377

Rubinstein, J. L., Ellsworth, W. L., McGarr, A., & Benz, H. M. (2014). The 2001–present induced earthquake sequence in the Raton Basin of northern New Mexico and southern Colorado. *Bulletin of the Seismological Society of America, 104(5)*, 2162–2181. https://doi.org/10.1785/0120140009

Roberts, N. S., Bell, A. F., & Main, I. G. (2015), Are volcanic seismic b-values high, and if so when? *J Volcanol Geotherm*, *Res 308*, 127–141. doi:10.1016/j.jvolgeores.2015.10.021

Scanlon, B. R., Weingarten, M. B., Murray, K. E., & Reedy, R. C. (2019). Managing Basin-Scale Fluid Budgets to Reduce Injection-Induced Seismicity from the Recent U.S. Shale Oil Revolution. *Seismolog. Res. Lett., 90*, 171−182.

Schoenball, M., Davatzes, N. C., & Glen, J. M. (2015). Differentiating induced and natural seismicity using space-time-magnitude statistics applied to the Coso Geothermal field. *Geophysical Research Letters*, *42*(15), 6221-6228.

Schoenball, M., & Ellsworth, W. L. (2017a). Waveform-relocated earthquake catalog for Oklahoma and southern Kansas illuminates the Regional Fault Network. *Seismological Research Letters, 88(5)*, 1252–1258. https://doi.org/10.1785/0220170083

Schoenball, M., & Ellsworth, W. L. (2017b). A systematic assessment of the spatiotemporal evolution of fault activation through induced seismicity in Oklahoma and Southern Kansas: Induced seismicity evolution in Oklahoma, *J. Geophys. Res., 122(12)*, 10189– 10206, doi: 10.1002/2017JB014850

Schoenball, M., Walsh, F. R., Weingarten, M., & Ellsworth, W. L. (2018). How faults wake up: the Guthrie-Langston, Oklahoma earthquakes. *The Leading Edge, 37(2)*, 100-106.

Schultz, R., Stern, V., & Gu, Y. J. (2014). An investigation of seismicity clustered near the Cordel Field, west central Alberta, and its relation to a nearby disposal well. *J. Geophys. Res. Solid Earth, 119*, 3410–3423, doi:10.1002/2013JB010836

Schwab, D. R., Bidgoli, T. S., & Taylor, M. H. (2017). Characterizing the potential for injection-induced fault reactivation through subsurface structural mapping and stress field analysis, Wellington Field, Sumner County, Kansas. *Journal of Geophysical Research: Solid Earth,* 122, 10,132–10,154. https://doi.org/10.1002/ 2017JB014071

Shen, L. W., Schmitt, D. R., Wang, R., & Hauck, T. E. (2021). States of in-situ stress in the Duvernay East Shale Basin and Willesden Green of Alberta, Canada: variable in-situ stress states effect fault stability. *Journal of Geophysical Research: Solid Earth*, e2020JB021221.

Skoumal, R. J., & Trugman, D. T. (2021). The proliferation of induced seismicity in the Permian Basin, Texas. *Journal of Geophysical Research: Solid Earth, 126*, e2021JB021921. https://doi. org/10.1029/2021JB021921

Skoumal, R. J., Barbour, A. J., Brudzinski, M. R., Langenkamp, T., & Kaven, J. O. (2020). Induced seismicity in the Delaware Basin, Texas. *Journal of Geophysical Research: Solid Earth, 125*, e2019JB018558. https://doi.org/ 10.1029/2019JB018558

Snoke, J. A. (2003). FOCMEC: Focal mechanism determinations. *International handbook of earthquake and engineering seismology, 85*, 1629-1630.

Treiman, J. A., Kendrick, K. J., Bryant, W. A., Rockwell, T. K., & McGill, S. F. (2002). Primary surface rupture associated with the *M* 7.1 16 October 1999 Hector Mine earthquake, San Bernardino County, California. *Bull. Seismol. Soc. Am.*, *92*, 1171-1191.

Trugman, D. T., & Shearer, P. M., (2017). GrowClust: A Hierarchical Clustering Algorithm for Relative Earthquake Relocation, with Application to the Spanish Springs and Sheldon, Nevada. *Earthquake Sequences. Seismol. Res. Lett. 88*, 379–391. doi:10.1785/0220160188

Verdecchia, A., Cochran, E. S., & Harrington, R. M. (2021). Fluid-earthquake and earthquake-earthquake interactions in southern Kansas, USA. *Journal of Geophysical Research: Solid Earth, 126*, e2020JB020384. https://doi.org/10.1029/2020JB020384

Walsh, R. R., & Zoback, M. D. (2015). Oklahoma's recent earthquakes and saltwater disposal, *Sci. Adv. 1*, e1500195, doi: 10.1126/sciadv.1500195

Weingarten, M., Ge, S., Godt, J. W., Bekins, B. A., & Rubinstein, J. L. (2015). High-rate injection is associated with the increase in U.S. mid-continent seismicity. *Science, 348(6241)*, 1336–1340. https://doi.org/10.1126/science.aab1345

Wang, R., Gu, Y. J., Schultz, R., Kim, A., and Atkinson G. (2016), Source analysis of a potential hydraulic fracturing induced earthquake near Fox Creek, Alberta, *Geophys. Res. Lett., 43*, 564-573, doi:10.1002/2015GL066917

Wang, R., Gu, Y. J., Schultz, R., & Chen, Y. (2018). Faults and non-double-couple components for induced earthquakes. Geophysical Research Letters, 45(17), 8966-8975.

Wang, R., Schmandt, B., Zhang, M., Glasgow, M., Kiser, E., Rysanek, S., & Stairs, R. (2020). Injection-induced earthquakes on complex fault zones of the Raton Basin illuminated by machine-learning phase picker and dense nodal array. *Geophysical Research Letters, 46*, e2020GL088168. https://doi.org/10.1029/2020GL088168

Wessel, P., & Smith, W. H. (1991). Free software helps map and display data. *Eos, Transactions American Geophysical Union, 72(41)*, 441–446. https://doi.org/10.1029/90EO00319

Woodward, L. A. (1997). Role of regional tectonic analysis in exploration for fracture reservoirs in Cretaceous source rocks of the Raton Basin, New Mexico. *Mountain Geologist , 34*, 73–80.

Zaliapin, I., & Ben-Zion Y. (2015). Artefacts of earthquake location er- rors and short-term incompleteness on seismicity clusters in southern California. *Geophys. J. Int.*, *202*, 1949–1968, doi: 10.1093/gji/ggv259

Zaliapin, I., & Ben-Zion, Y. (2016). Discriminating characteristics of tectonic and human-induced seismicity. *Bull. Seismol. Soc. Am. 106(3)*, 846–859, doi: 10.1785/0120150211

Zaliapin, I., Gabrielov, A., Keilis-Borok, V., & Wong H. (2008). Clustering analysis of seismicity and aftershock identification. *Phys. Rev. Lett. 101(1)*, 018501, doi: 10.1103/ PhysRevLett.101.018501

Zhang, M., Ellsworth, W. L., & Beroza, G. C. (2019). Rapid Earthquake Association and Location. *Seismological Research Letters, 90(6)*, 2276-2284.

Zhu, W., & Beroza, G. C. (2019). PhaseNet: a deep-neural-network-based seismic arrival-time picking method. *Geophysical Journal International, 216(1)*, 261-273.